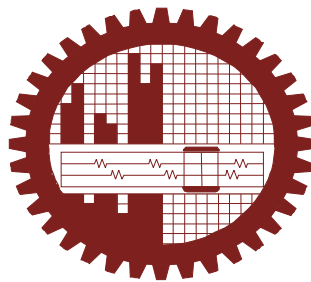


**STRUCTURAL, DIELECTRIC AND MAGNETIC PROPERTIES OF Gd AND
Ti CO-DOPED BiFeO₃ MULTIFERROICS AT ROOM TEMPERATURE**

M.Phil Thesis
(Physics)

Md. Oyes Kurni
Roll No.: 0412143017F
Session: April/ 2012



Department of Physics
Bangladesh University of Engineering & Technology
Dhaka 1000, Bangladesh

STRUCTURAL, DIELECTRIC AND MAGNETIC PROPERTIES OF Gd AND Ti CO-DOPED BiFeO₃ MULTIFERROICS AT ROOM TEMPERATURE

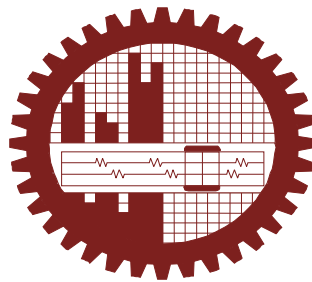
A Dissertation Submitted to the Department of Physics, Bangladesh University of Engineering & Technology, Dhaka in Partial Fulfillment of Requirement for the Degree of Master of Philosophy in Physics

By

Md. Oyes Kurni

Roll No.: 0412143017F

Session: April/ 2012



Department of Physics
Bangladesh University of Engineering & Technology
Dhaka 1000, Bangladesh

Declaration

This thesis is a presentation of my original research work. Wherever contributions of others are involved, every effort is made to indicate this clearly, with due reference to the literature, and acknowledgement of collaborative research and discussions. The work was done under the guidance of Dr. Mohammed Abdul Basith, at the Department of Physics, Bangladesh University of Engineering & Technology, Dhaka, Bangladesh.



Md. Oyes Kurni
Roll No.: 0412143017F
Session: April/2012
BUET, Dhaka.


**BANGLADESH UNIVERSITY OF ENGINEERING & TECHNOLOGY (BUET), DHAKA
DEPARTMENT OF PHYSICS**




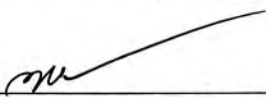
CERTIFICATION OF THESIS

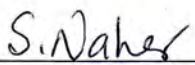
The thesis titled “**STRUCTURAL, DIELECTRIC AND MAGNETIC PROPERTIES OF Gd AND Ti CO-DOPED BiFeO₃ MULTIFERROICS AT ROOM TEMPERATURE**” submitted by Md. Oyes Kurni, Roll No-0412143017F, Registration No-0412143017F, Session: April-2012, has been accepted as satisfactory in partial fulfillment of the requirement for the degree of **Master of Philosophy (M. Phil.)** in Physics on 06 December, 2015.

BOARD OF EXAMINERS

1. 

Dr. Mohammed Abdul Basith
Associate Professor
Department of Physics, BUET, Dhaka. Chairman
(Supervisor)
2. 

Dr. Afia Begum
Professor & Head
Department of Physics, BUET, Dhaka. Member
(Ex-Officio)
3. 

Dr. Md. Abu Hashan Bhuiyan
Professor
Department of Physics, BUET, Dhaka. Member
4. 

Dr. Shumsun Naher Begum
Professor
Department of Physics
Shahjalal University of Science & Technology, Sylhet Member
(External)

Dedicated
To
My Father

Acknowledgements

First of all, I would like to express all of my affection and glorification to the almighty Allah, who has enabled me to perform this research work and as well as to submit this thesis.

I express my unlimited gratitude to my honorable supervisor Dr. Mohammed Abdul Basith, Associate Professor, Department of Physics, BUET, for his supervision, constant enormous valuable advice, guidance, and inspiration in pursuing the whole investigation of the present research work. He is very experienced in guiding thesis and has profound knowledge in multiferroic material systems. Words are always insufficient to express his working capacities and unending enthusiasm for scientific rigorousness for innovative investigations. The same time, he has excellent personal character. This always becomes the everlasting source of inspiration for his students. I am really honored to have Dr. Mohammed Abdul Basith as my supervisor. I can honestly say that I would never have been able to accomplish my thesis work without the support from him. All these give me a very good environment to finish my thesis.

I am exceedingly grateful to Professor, Dr. Afia Begum, Head, Department of Physics, BUET, for her kind permission to do this research work. I am also grateful to BUET authority for providing the financial grant for this research.

I would like to express my special gratitude to Professor Dr. Md. Abu Hashan Bhuiyan, Professor Dr. Md. Feroz Alam Khan, and all other respected teachers of the Department of Physics, BUET for their cooperation.

I am grateful to the ministry of Science and technology, Bangladesh, and Graduate School of Science and Engineering, Yamagata University, Japan, for granting me NST Fellowship and technical assistance, respectively.

I am also gratefully acknowledge the wishes of my younger researchers Saiful, Atiq, Popy, Areef, Babu, Armeen, Tamanna, Abu Heena, for their constant support and care which always let me feel warm and happy.

Finally, I would like to take this opportunity to thank my family, specially my mother Mrs. Ambia Khatun and my wife Mrs. Jui. My family members have given me a strong foundation of emotional reinforcement and provide me with support and encouragement throughout my study. They kept me motivated to finish the research work as well and have been a source of added support.

Thanks all the others who did contributions during the thesis work.

Abstract

Structural, dielectric and magnetic properties of BiFeO₃ multiferroic samples, co-doped with magnetic Gd and non-magnetic Ti in place of Bi and Fe, respectively, were reported at room temperature. The nominal compositions of Bi_{0.9}Gd_{0.1}Fe_{1-x}Ti_xO₃ (x = 0.00 - 0.25) ceramics were synthesized by conventional solid state reaction technique. X-ray diffraction patterns revealed that the substitution of Fe by Ti induces a phase transition from rhombohedral to orthorhombic at x > 0.20. Morphological studies demonstrated that the average grain size was reduced from ~1.5 μm to ~200 nm with the increase in Ti content. Due to Ti substitution, the dielectric constant was stable over a wide range of high frequencies (30 kHz to 20 MHz) by suppressing the dispersion at low frequencies. The dielectric properties of the compounds are associated with their improved morphologies and reduced leakage current densities probably due to the lower concentration of oxygen vacancies in the compositions. Magnetic properties of Bi_{0.9}Gd_{0.1}Fe_{1-x}Ti_xO₃ (x = 0.00 - 0.25) ceramics measured at room temperature were enhanced with Ti substitution up to 20% compared to that of pure BiFeO₃ and Ti undoped Bi_{0.9}Gd_{0.1}FeO₃ samples. The enhanced magnetic properties might be attributed to the substitution induced suppression of spiral spin structure of BiFeO₃. An asymmetric shift both in the field and magnetization axes of magnetization versus magnetic field curves was observed. This indicates the presence of exchange bias effect in these compounds notably at room temperature.

Contents

Title.....	i
Declaration.....	ii
Certification.....	iii
Dedication.....	iv
Acknowledgements.....	v
Abstract.....	vi
Contents.....	vii
List of Figures.....	x
List of Tables.....	xiii

Chapter 1 Introduction [1-6]

1.1 Introduction	1
1.2 Aim of the Thesis.....	3
1.3 Outline of the Thesis.....	3
Reference:.....	4

Chapter 2 Theoretical Background [7-34]

2.1 Magnetism.....	7
2.1.1 Origin of Magnetism	7
2.1.2 Types of Magnetism.....	8
2.1.3 Magnetization.....	10
2.1.4 Magnetic Moment.....	10
2.1.4.1 Magnetic Moment of an Atom.....	10
2.1.4.2 Magnetic Moment of an Electron	11
2.1.5 The Hysteresis Loop.....	12
2.1.6 Magnetic Domains.....	13

2.1.7 Curie's Law	14
2.1.8 Curie-Weiss Law	14
2.2 Ferroelectricity	15
2.2.1 Classification of Ferroelectrics	16
2.2.2 Perovskite	17
2.2.2.1 Structure and Properties of Perovskite	17
2.2.2.2 The Deformation of Perovskite.....	18
2.3 Dielectrics.....	18
2.3.1 Dielectric Polarization	19
2.3.2 Dielectric Constant	22
2.3.3 Dielectric Loss	23
2.3.4 Dependence of Dielectric Constant on Frequency	24
2.4 Magnetoelectric Effect.....	25
2.5 Multiferroics	26
2.5.1 Different Types of Multiferroics.....	27
2.5.2 BiFeO ₃ Multiferroic.....	29
2.5.3 Recent Progress of Multiferroics	30
Reference:.....	31

Chapter 3

Experimental Details [35-49]

3.1 Sample Preparation	35
3.1.1 Solid State Reaction Technique:	35
3.1.2 Calcination	36
3.1.3 Pelletization.....	37
3.1.4 Sintering	37
3.2 Synthesis of Composition.....	38
3.3 Characterization Techniques	39
3.3.1 X-Ray Diffraction Analysis	39

3.3.2 Scanning Electron Microscope (SEM).....	41
3.3.2.1 Scanning Process and Image Formation	42
3.3.2.2 Energy Dispersion X-Ray Spectroscopy.....	43
3.3.3 X-Ray Photoelectron Spectroscopy (XPS)	44
3.3.4 Dielectric Properties Measurement.....	46
3.3.5 Magnetic Properties Measurement	47
Reference:.....	49

Chapter 4

Results and Discussion [50-67]

4.1 Structural Characterizations.....	50
4.1.1 X-Ray Diffraction	50
4.1.2 Morphological Studies.....	52
4.1.3 XPS Analysis	54
4.2 Dielectric Measurement.....	56
4.3 Magnetic Characterization	59
Reference:.....	65

Chapter 5

Conclusions [68-70]

5.1 Conclusions	68
5.2 Future work	68
Reference:.....	70

List of Figures

Figure 2.1	The orbit of a spinning electron about the nucleus of an atom.	7
Figure 2.2	Two typical hysteresis loops - the left loop shows some permanently magnetic material, the right loop a softer magnet. The solid blue line indicates reducing field, the dashed red line indicates increasing field.	12
Figure 2.3	Illustration of domains in magnetic materials.	13
Figure 2.4	P-E Relationships.	15
Figure 2.5	Schematic illustration of the ABO_3 perovskite structure.	17
Figure 2.6	The bound charges are the charges that are touching the capacitor plates, while the free charges usually float around in the material, but for this case, they are aligned with the bound charges.	19
Figure 2.7	The effect of an external electric field on an ionic material. The positive charges will flow with the field and the negative charges will flow against the field, causing a net average dipole moment per ion to form.	20
Figure 2.8	This shows how the free positive charges inside the dielectric material migrate towards the negative charge build-up on the right, caused by the external electric field.	22
Figure 2.9	Multiferroics combine the properties of ferroelectrics and magnets (green). In the ideal case, the magnetization of a ferromagnet in a magnetic field displays the usual hysteresis (blue), and ferroelectrics have a similar response to an electric field (yellow).	27
Figure 3.1	Flow chart of solid state reaction technique.	35
Figure 3.2	Schematic representation of sintering stages: (a) green body, (b) initial stage, (c) intermediate stage, and (d) final stage.	38
Figure 3.3	Bragg's law of diffraction.	40
Figure 3.4	The schematic diagram shows the operation of XRD.	40

Figure 3.5	X-ray diffraction analysis machine.	41
Figure 3.6	Photograph of Scanning Electron Microscope (SEM).	42
Figure 3.7	Principle of EDX.	44
Figure 3.8	Schematic diagram of a typical X-ray photoelectron spectroscopy (XPS).	45
Figure 3.9	Diagram of a dielectric plate.	47
Figure 3.10	The Lakeshore vibrating sample magnetometer (VSM).	58
Figure 4.1 (a)	X-ray diffraction patterns of $\text{Bi}_{0.9}\text{Gd}_{0.1}\text{Fe}_{1-x}\text{Ti}_x\text{O}_3$ ($x = 0.00 - 0.25$) ceramics.	51
Figure 4.1 (b)	Splitting of peak around $2\theta \approx 32^\circ$ as Ti content increases to $x = 0.25$.	51
Figure 4.2	FESEM micrograph of $\text{Bi}_{0.9}\text{Gd}_{0.1}\text{Fe}_{1-x}\text{Ti}_x\text{O}_3$ ceramics: (a) $x = 0.00$, (b) $x = 0.10$ and (c) $x = 0.25$. Inset: respective histograms of images (a) and (b). (d) Shows an EDX pattern recorded from image (b).	53
Figure 4.3 (a)	XPS spectra of $\text{Bi}_{0.9}\text{Gd}_{0.1}\text{Fe}_{0.9}\text{Ti}_{0.1}\text{O}_3$ ceramic system as a representative of other compositions.	55
Figure 4.3 (b)	The O 1s core spectrum and oxygen vacancy peaks for all compositions.	55
Figure 4.4 (a)	Semi-log plot of dielectric constant of $\text{Bi}_{0.9}\text{Gd}_{0.1}\text{Fe}_{1-x}\text{Ti}_x\text{O}_3$ ceramics: (a) $x = 0.00$ (b) $x = 0.05$ (c) $x = 0.10$ (d) $x = 0.15$ (e) $x = 0.20$ and (f) $x = 0.25$ recorded at RT in the wide frequency range from 100 Hz to 20 MHz.	56
Figure 4.4 (b)	Variation in $\tan\delta$ as a function of frequency at RT.	66
Figure 4.5	(a) M-H hysteresis loops of pure BiFeO_3 and $\text{Bi}_{0.9}\text{Gd}_{0.1}\text{Fe}_{1-x}\text{Ti}_x\text{O}_3$ ($x = 0.00 - 0.25$) ceramics at room temperature. (b) An enlarged view of the low-field M-H hysteresis loop of pure BiFeO_3 . (c) – (h) An enlarged view of the low-field M-H hysteresis loops of $\text{Bi}_{0.9}\text{Gd}_{0.1}\text{Fe}_{1-x}\text{Ti}_x\text{O}_3$ samples obtained at RT: (c) $x = 0.00$ (d) $x = 0.05$ (e) $x = 0.10$ (f) $x = 0.15$ (g) $x = 0.20$ and (h) $x = 0.25$. (h) Also shows the left and right side coercive fields (H_{c1} and H_{c2})	60

	and remanent magnetizations (M_{r1} and M_{r2}) of M-H loops. An asymmetric shifts both in the field and magnetization axes of Gd and Ti co-doped samples (d)-(h) indicates the existence of the EB phenomenon.	
Figure 4.6	Variation of (a) remanent magnetization and (b) coercive fields at RT, respectively, in $\text{Bi}_{0.9}\text{Gd}_{0.1}\text{Fe}_{1-x}\text{Ti}_x\text{O}_3$ ($x = 0.00 - 0.25$) as a function Ti concentration.	62
Figure 5.1	XPS spectra of the O 1s of $\text{Bi}_{0.9}\text{Gd}_{0.1}\text{Fe}_{1-x}\text{Ti}_x\text{O}_3$ ($x = 0.00 - 0.20$) (a) bulk polycrystalline materials and (b) nanoparticles obtained after a sonication time of 60 minutes. The oxygen related defects were completely reduced in the synthesized nanoparticles.	69

List of Tables

Table 4.1	Dielectric constant at different frequencies for $x = 0.00 - 0.25$. The table shows that in a wide range of high frequencies (50 kHz to 20000 kHz) the dielectric constant amongst co-doped ceramics is higher for $x = 0.10, 0.15$ and 0.20 compared to that of $x = 0.05$ and 0.25 samples.	58
Table 4.2	The table shows the calculated values of H_{EB} and M_{EB} for $Bi_{0.9}Gd_{0.1}Fe_{1-x}Ti_xO_3$ ceramics observed at RT. Table also demonstrates comparison of the H_{EB} for $La_{0.8}Bi_{0.2}Fe_{1-x}Mn_xO_3$ multiferroics observed at 200K (Ref. 21) and $Bi_{0.9}Gd_{0.1}Fe_{1-x}Ti_xO_3$ ceramics observed at RT.	64

Chapter 1

Introduction

1.1 Introduction

Multiferroic materials exhibit ferroelectric (or antiferroelectric) properties in combination with ferromagnetic (or antiferromagnetic) properties in the same phase and have attracted considerable research interest due to their potential applications in multiple state memory elements, magnetic field sensor and electric field controlled ferromagnetic resonance devices [1-7]. Amongst the multiferroic ceramics being widely investigated, BiFeO₃ is a promising candidate for novel applications which allow mutual control of the electric polarization with a magnetic field and magnetization by an electric field [6,7]. The multiferroic BiFeO₃ is ferroelectric below $T_C \sim 1103\text{K}$ and antiferromagnetic below $T_N \sim 653\text{K}$, having rhombohedrally distorted perovskite ABO₃ (A = Bi, B = Fe) structure [4]. Previous investigations revealed that pure phase of BiFeO₃ is difficult to obtain [8,9] and various impurity phases of bulk BiFeO₃ have been reported, mainly comprising of Bi₂Fe₄O₉, Bi₃₆Fe₂₄O₅₇ and Bi₂₅FeO₄₀ [10,11].

In BiFeO₃, magnetic ordering is of antiferromagnetic type, having a spiral modulated spin structure (SMSS) with an incommensurate long-wavelength period of 62 nm [12]. This spiral spin structure cancels the macroscopic magnetization and prevents the observation of the linear magnetoelectric effect [13-15]. In addition, the bulk BiFeO₃ is characterized by serious current leakage problems due to the existence of a large number of charge centre's caused by oxygen ion vacancies [12]. These problems limit the use of BiFeO₃ for fabrication of multifunctional devices [16]. In order to overcome these problems, many attempts have been undertaken [12]. Amongst which the partial substitution of Bi³⁺ by ions such as Sm³⁺ [17,18], Nd³⁺ [19,20] etc., and also substitution of Fe³⁺ by ions such as Cr³⁺ [21], or simultaneous minor substitution of Bi³⁺ and Fe³⁺ by ions such as La³⁺ and Mn³⁺ or La³⁺ and Ti⁴⁺, respectively [4,12] improved the magnetism and ferroelectricity in BiFeO₃. The partial substitution of Bi³⁺ with ions having the biggest ionic radius has been found to effectively suppress the spiral spin structure of BiFeO₃ giving rise to the appearance of weak ferromagnetism [22].

Among various kind of doping at A site, it was observed that the substitution of 10% Gd in place of Bi enhanced the room temperature magnetization of BiFeO₃ [6, 23] as well as improved the phase purity of bulk BiFeO₃. At B site, the partial substitution of Fe by Ti is found specially attractive as the substitution of Ti⁴⁺ decreased the leakage current significantly and induced a remanent magnetization in BiFeO₃ [11,24]. It is observed that at 200K due to the substitution of Fe by Ti in BiFe_{0.75}Ti_{0.25}O₃, the area of the magnetization versus magnetic field (M-H) curve increased compared to that of pure BiFeO₃. However, at room temperature, the M-H loop was still very narrow [11] which indicates that substitution of 25% Ti in place of Fe cannot improve notably the magnetic properties at room temperature (RT). Therefore, in the present investigation, we intend to study the effect of co-substitution of magnetic Gd and non-magnetic Ti in place of Bi and Fe, respectively, in BiFeO₃ samples. So far there are reports on the co-doping effect of La³⁺ and Ti⁴⁺ [12], La³⁺ and Mn³⁺ [4], La³⁺ and V⁵⁺ [25], respectively, in place of Bi and Fe in BiFeO₃. To the best of our knowledge, there was no published data on dielectric and magnetic properties of Gd and Ti co-doped BiFeO₃ samples measured at RT until we have published our results in the Journal of Applied Physics in January 2014 [27]. Later on, in September 2014, another group also investigated the dielectric, magnetic and optical properties of Gd and Ti co-doped BiFeO₃ system prepared by solid state reaction technique [28].

In the present investigation, nominal compositions of Bi_{0.9}Gd_{0.1}Fe_{1-x}Ti_xO₃ (x = 0.00 – 0.25) ceramics were synthesized by conventional solid state reaction technique and their structure, morphology, dielectric, and magnetic properties were investigated. Investigation of the surface morphology and the structure of the samples were done by using scanning electron microscopy (SEM) and X-ray diffraction techniques, respectively. The dielectric properties of the multiferroics were observed as a function of frequency at room temperature, and the measurements of magnetic properties of the samples were done by using vibrating sample magnetometer (VSM) at room temperature. We observed that due to the combined effects of Gd and Ti on BiFeO₃ multiferroics, the dielectric and magnetic properties of these ceramics were improved at RT. Moreover, an asymmetry exhibiting shifts both in the field and magnetization axes of M-H curves was

also observed in Gd and Ti co-doped ceramics which indicates the presence of exchange bias (EB) effect in these compounds at RT.

1.2 Aim of the Thesis

The main objectives of the present research are as follows:

- (a) Preparation of various compositions of $\text{Bi}_{0.9}\text{Gd}_{0.1}\text{Fe}_{1-x}\text{Ti}_x\text{O}_3$ ($x = 0.0, 0.05, 0.1, 0.15, 0.2, 0.25$) multiferroics by using solid state reaction method.
- (b) Investigation of the surface morphology and the structure of the samples using scanning electron microscopy (SEM) and X-ray diffraction techniques, respectively.
- (c) Investigation of the concentration of oxygen vacancies in each composition using X-ray photoelectron spectroscopy (XPS) technique.
- (d) Investigation of the dielectric properties of the multiferroics as a function of frequency at room temperature.
- (e) Measurements of the magnetic properties such as remanent magnetization (M_r), coercivity (H_c) with different compositions from M-H curves obtained from vibrating sample magnetometer (VSM) at room temperature.

1.3 Outline of the Thesis

The thesis is organized as follows:

- ⇒ Chapter 1 of this thesis deals with the importance of multiferroics and objectives of the present work.
- ⇒ Chapter 2 gives a brief overview of the materials and, as well as the theoretical background.
- ⇒ Chapter 3 provides the details of the sample preparation, and the description of different measurement techniques that have been used in this research work.
- ⇒ Chapter 4 is devoted to the results of various investigations of the study and explanation of results in the light of existing theories.
- ⇒ The conclusions drawn from the overall experimental results and discussion are presented in Chapter 5.

Reference:

- [1] Eerenstein, W., Mathur, N. D., Scott, J. F., “Multiferroic and magnetoelectric materials”, *Nature* 442, pp-759-765, 2006.
- [2] Cheong, S. W., Mostovoy, M., “Multiferroics: a magnetic twist for ferroelectricity”, *Nature Materials* 6, pp-13–20, 2007.
- [3] Ramesh, R., “Emerging routes to multiferroics”, *Nature* 461, pp-1218-1219, 2009.
- [4] Anjum, G., Kumar, R., Mollah, S., Shukla, D. K., Kumar, S., Lee, C. G., “Structural, dielectric, and magnetic properties of $\text{La}_{0.8}\text{Bi}_{0.2}\text{Fe}_{1-x}\text{Mn}_x\text{O}_3$ ($0.0 \leq x \leq 0.4$) multiferroics”, *J. App. Phys.*, Vol-107, pp-103916-103924, 2010.
- [5] Silva, J., Reyes, A., Esparza, H., Camacho, H., and Fuentes, L., “ BiFeO_3 : A review on synthesis, doping and crystal structure”, *Integrated Ferroelectrics*, Vol. 126, pp-47-59, 2011.
- [6] Lazenka, V. V., Zhang, G., Vanacken, J., Makoed, I. I., Ravinski, A. F., Moshchalkov, V. V., “Structural transformation and magnetoelectric behaviour in $\text{Bi}_{1-x}\text{Gd}_x\text{FeO}_3$ multiferroics”, *J. Phys. D: Appl. Phys.*, Vol-45, pp-125002-125009, 2012.
- [7] Tirupathi, P., and Chandra, A., “Stabilization of dielectric anomaly near the magnetic phase transition in Ca^{2+} doped BiFeO_3 multifunctional ceramics”, *J. of Alloys and Compounds*, Vol. 564, pp-151-157, 2013.
- [8] Jiang, Q.H., Nan, C.W., *J. Am. Ceram.*, “Synthesis and Properties of Multiferroic La Modified BiFeO_3 Ceramics”, *J. Am. Ceram. Soc.* 89, pp2123-2127, 2006.
- [9] Ghosh, S., Dasgupta, S., Sen, A., Maiti, H. S., “Low-Temperature Synthesis of Bismuth Ferrite by Soft Chemical Route”, *J. Am. Ceram. Soc.*, Vol-88, pp-1349-1352, 2005.
- [10] Munoz, T., Rivera, J. P., Monnier, A., and Schmid, H., “Measurement of the Quadratic Magnetoelectric Effect on Single Crystalline BiFeO_3 ”, *Jpn. J. Appl. Phys.*, Part 1 24, pp1051-1053, 1985.
- [11] Kumar, M., Yadav, K.L., “Study of room temperature magnetoelectric coupling in Ti substituted bismuth ferrite system”, *J. Appl. Phys.* 100, pp074111-074114, 2006.

- [12] Agarwal, R. A., Ashima, S. S., and Ahlawat, N., “Structural transformation and improved dielectric and magnetic properties in Ti-substituted $\text{Bi}_{0.8}\text{La}_{0.2}\text{FeO}_3$ multiferroics”, *J. Phys. D: Appl. Phys.* 45, pp165001- 165010, 2012.
- [13] Catalan and Scott, J. F., “Physics and Applications of Bismuth Ferrite”, *Adv. Mater.* 21, 2463, 2009.
- [14] Sosnowska, I., Neumaier, T. P., and Steichele, E., “Spiral magnetic ordering in bismuth ferrite”, *J. Phys. C: Solid State Phys.* 15, 4835, 1982.
- [15] Ederer, C., and Spaldin, N. A., “Weak ferromagnetism and magnetoelectric coupling in bismuth ferrite”, *Phys. Rev. B* 71, 060401(R), 2005.
- [16] Yuan, G. L., Kishi, K. Z. B., Liu, J. M., Or, S. W. , Wang, Y. P. and Liu, Z. G., “Multiferroic Properties of Single-Phase $\text{Bi}_{0.85}\text{La}_{0.15}\text{FeO}_3$ Lead-Free Ceramics”, *J. Am. Ceram. Soc.* 89, pp 3136-3139, 2006.
- [17] Khomchenko, V. A., Paixao, J. A., Shvartsman, V. V., Borisov, P. , Kleemann, W., Karpinsky, D. V., Kholkin, A. L. “Effect of Sm substitution on ferroelectric and magnetic properties of BiFeO_3 ”, *Scripta Materialia*, 62, pp 238-241, 2010.
- [18] Khomchenko, V. A., Paixao, J. A., Costa, B. F. O., Karpinsky, D.V., Kholkin, A. L., Troyanchuk, I. O., Shvartsman, V. V., Borisov, P., Kleeman, W. , “Structural, ferroelectric and magnetic properties of $\text{Bi}_{0.85}\text{Sm}_{0.15}\text{FeO}_3$ perovskite”, *Crystal Research and Technology*, 46, 238-242, 2011.
- [19] Mishra, R., Pradhan, D., Choudhary, R., Banerjee, A., “Dipolar and magnetic ordering in Nd- modified BiFeO_3 nanoceramics”, *J. Magn. Magn. Mater.*,320, pp 2602-2607, 2008.
- [20] Gaur, A., Singh, P., Choudhary, N., Kumar, D., Shariq, M., Singh, K., Kaur, N. , Kaur, D. , “Structural, optical and magnetic properties of Nd-doped BiFeO_3 thin films prepared by pulsed laser deposition”, *Physica B: Condensed Matter*, 406, pp 1877-1882, 2011.
- [21] Chang, F., Zhang, N., Yang, F., Wang, S., Song, G., “Effect of Cr substitution on the structure and electrical properties of BiFeO_3 ceramics”, *J. Phys. D: Appl. Phys.*, 40, 7799-7803, 2007.
- [22] Khomchenko, V. A., Kopcewicz, M., Lopes, A. M. L., Pogorelov, Y. G., Araujo, J. P., Vieira, J. M., and Kholkin, A. L., “Intrinsic nature of the magnetization

- enhancement in heterovalently doped $\text{Bi}_{1-x}\text{A}_x\text{FeO}_3$ (A= Ca, Sr, Pb, Ba) multiferroics”, *J. Phys. D: Appl. Phys.* 41, 102003, 2008.
- [23] Uniyal, P., Yadav, K.L., “Study of dielectric, magnetic and ferroelectric properties in $\text{Bi}_{1-x}\text{Gd}_x\text{FeO}_3$ ”, *Materials Letters* 62, pp 2858-2861, 2008.
- [24] Wang, Y., and Nan, C. W., “Enhanced ferroelectricity in Ti-doped multiferroic BiFeO_3 thin films”, *Appl. Phys. Lett.* 89, 052903, 2006.
- [25] Yu, B., Li, M., Liu, J., Guo, D., Pei, L., and Zhao, X., “Structural, morphological and piezoresponse studies of Pr and Sc co-substituted BiFeO_3 ceramics”, *J. Phys. D* 41, 185401, 2008.
- [26] Yu, B., Li, M., Liu, J., Guo, D., Pei, L., and Zhao, X., “Structural, morphological and piezoresponse studies of Pr and Sc co-substituted BiFeO_3 ceramics”, *J. Phys. D* 41, 185401, 2008.
- [27] Basith, M. A., Kurni, O., Alam, M. S., Sinha, B. L. and Bashir Ahmmad, “Room temperature dielectric and magnetic properties of Gd and Ti co-doped BiFeO_3 ceramics”, *J. Appl. Phys.*, 115, 024102–024107, 2014.
- [28] Manoj, K., Prakash, C. S., Sandeep, C., “Electron spin resonance study and improved magnetic and dielectric properties of Gd–Ti co-substituted BiFeO_3 ceramics”, *J Mater Sci: Mater Electron*, 25:5366–5374, 2014.

Chapter 2

Theoretical Background

2.1 Magnetism

Magnetism is a force generated in matter by the motion of electrons within its atoms. Magnetism and electricity represent different aspects of the force of electromagnetism, which is one part of Nature's fundamental electroweak force [1]. The region in space that is penetrated by the imaginary lines of magnetic force describes a magnetic field. The strength of the magnetic field is determined by the number of lines of force per unit area of space. Magnetic fields are created on a large scale either by the passage of an electric current through magnetic metals or by magnetized materials called magnets. The elemental metals-iron, cobalt, nickel, and their solid solutions or alloys with related metallic elements are typical materials that respond strongly to magnetic fields. Unlike the all pervasive fundamental force field of gravity, the magnetic force field within a magnetized body, such as a bar magnet, is polarized that is, the field is strongest and of opposite signs at the two extremities or poles of the magnet.

2.1.1 Origin of Magnetism

Magnetism arises from two types of motions of electrons in atoms - one is the motion of the electrons in an orbit around the nucleus, similar to the motion of the planets in our solar system around the sun, and the other is the spin of the electrons around its axis, analogous to the rotation of the Earth about its own axis.

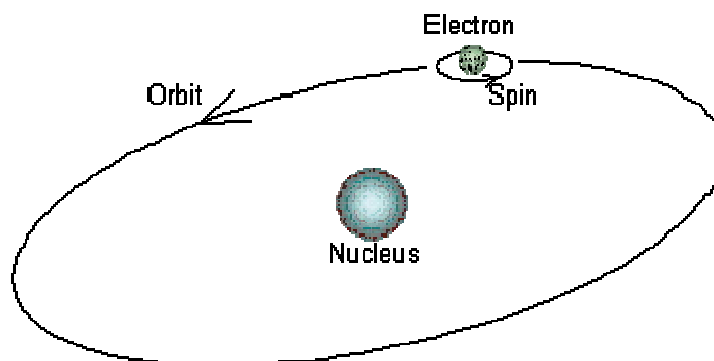


Figure 2.1: The orbit of a spinning electron about the nucleus of an atom.

The orbital and the spin motion independently impart a magnetic moment on each electron causing each of them to behave as a tiny magnet [2]. The magnetic moment of a magnet is defined by the rotational force experienced by it in a magnetic field of unit strength acting perpendicular to its magnetic axis. In a large fraction of the elements, the magnetic moment of the electrons cancel out because of the Pauli exclusion principle, which states that each electronic orbit can be occupied by only two electrons of opposite spin. However, a number of so-called transition metal atoms, such as iron, cobalt, and nickel, have magnetic moments that are not cancelled; these elements are, therefore, common examples of magnetic materials. In these transition metal elements the magnetic moment arises only from the spin of the electrons. In the rare earth elements (that begin with lanthanum in the sixth row of the Periodic Table of Elements), however, the effect of the orbital motion of the electrons is not cancelled, and hence both spin and orbital motion contribute to the magnetic moment. Examples of some magnetic rare earth elements are: cerium, neodymium, samarium, and europium. In addition to metals and alloys of transition and rare earth elements, magnetic moments are also observed in a wide variety of chemical compounds involving these elements. Among the common magnetic compounds are the metal oxides, which are chemically bonded compositions of metals with oxygen.

2.1.2 Types of Magnetism

Five basic types of magnetism have been observed and classified on the basis of the magnetic behavior of materials in response to magnetic fields at different temperatures. These types of magnetism are: ferromagnetism, ferrimagnetism, antiferromagnetism, paramagnetism, and diamagnetism.

Ferromagnetism and ferrimagnetism occur when the magnetic moments in a magnetic material line up spontaneously at a temperature below the so-called Curie temperature, to produce net magnetization. The magnetic moments are aligned at random at temperatures above the Curie point, but become ordered, typically in a vertical or, in special cases, in a spiral (helical) array, below this temperature [3]. In a ferromagnet magnetic moments of equal magnitude arrange themselves in parallel to each other. In a ferrimagnet, on the other hand, the moments are unequal in magnitude and order in an antiparallel

arrangement. When the moments are equal in magnitude and ordering occurs at a temperature called the Neel temperature in an antiparallel array to give no net magnetization, the phenomenon is referred to as antiferromagnetism. These transitions from disorder to order represent classic examples of phase transitions. Another example of a phase transition is the freezing of the disordered molecules of water at a critical temperature of 32° F (0° C) to form the ordered structure of ice. The magnetic moments referred to as spins are localized on the tiny electronic magnets within the atoms of the solid. Mathematically, the electronic spins are equal to the angular momentum (the rotational velocity times the moment of inertia) of the rotating electrons. The spins in a ferromagnetic or a ferrimagnetic single crystal undergo spontaneous alignment to form a macroscopic (large scale) magnetized object. Most magnetic solids, however, are not single crystals, but consist of single crystal domains separated by domain walls. The spins align within a domain below the Curie temperature, independently of any external magnetic field, but the domains have to be aligned in a magnetic field in order to produce a macroscopic magnetized object. This process is effected by the rotation of the direction of the spins in the domain wall under the influence of the magnetic field, resulting in a displacement of the wall and the eventual creation of a single large domain with the same spin orientation.

Paramagnetism is a weak form of magnetism observed in substances which display a positive response to an applied magnetic field. This response is described by its magnetic susceptibility per unit volume, which is a dimensionless quantity defined by the ratio of the magnetic moment to the magnetic field intensity. Paramagnetism is observed, for example, in atoms and molecules with an odd number of electrons, since here the net magnetic moment cannot be zero. Diamagnetism is associated with materials that have a negative magnetic susceptibility. It occurs in nonmagnetic substances like graphite, copper, silver and gold, and in the superconducting state of certain elemental and compound metals. The negative magnetic susceptibility in these materials is the result of a current induced in the electron orbits of the atoms by the applied magnetic field. The electron current then induces a magnetic moment of opposite sign to that of the applied field. The net result of these interactions is that the material is shielded from penetration by the applied magnetic field.

2.1.3 Magnetization

The process of making a substance temporarily or permanently magnetic, as by insertion in a magnetic field is known as magnetization. Magnetization is defined as the quantity of magnetic moment per unit volume. It is represented by a vector M . The origin of the magnetic moments responsible for magnetization can be either microscopic electric currents resulting from the motion of electrons in atoms, or the spin of the electrons or the nuclei. Net magnetization results from the response of a material to an external magnetic field, together with any unbalanced magnetic dipole moments that may be inherent in the material itself; for example, in ferromagnets. Magnetization is not always homogeneous within a body, but rather varies between different points. Magnetization also describes how a material responds to an applied magnetic field as well as the way the material changes the magnetic field, and can be used to calculate the forces that result from those interactions. It can be compared to electric polarization, which is the measure of the corresponding response of a material to an electric field in electrostatics.

2.1.4 Magnetic Moment

The magnetic moment of a magnet is a quantity that determines the torque it will experience in an external magnetic field. A loop of electric current, a bar magnet, an electron (revolving around a nucleus), a molecule, and a planet all have magnetic moments.

2.1.4.1 Magnetic Moment of an Atom

For an atom, individual electron spins are added to get a total spin, and individual orbital angular momenta are added to get a total orbital angular momentum. These two then are added using angular momentum coupling to get a total angular momentum. The magnitude of the atomic dipole moment is then,

$$m_{\text{Atom}} = g_i \mu_B \sqrt{j(j+1)} \quad \dots \quad \dots \quad \dots \quad \dots \quad \dots \quad \dots \quad \dots \quad (2.1)$$

Where, J is the total angular momentum quantum number, g_i is the Landé g -factor, and μ_B is the Bohr magnetron [4]. The component of this magnetic moment along the direction of the magnetic field is then,

$$m_{\text{Atom}}(z) = -mg_j\mu_B \quad \dots \quad \dots \quad \dots \quad \dots \quad \dots \quad \dots \quad \dots \quad (2.2)$$

Where, m is called the magnetic quantum number or the equatorial quantum number [5], which can take on any of $2J+1$ values [6]:

$$-J, -(J-1) \dots \dots 0 \dots \dots + (J-1), +J$$

The negative sign occurs because electrons have negative charge.

Due to the angular momentum, the dynamics of a magnetic dipole in a magnetic field differs from that of an electric dipole in an electric field. The field does exert a torque on the magnetic dipole tending to align it with the field. However, torque is proportional to rate of change of angular momentum, so precession occurs: the direction of spin changes.

This behavior is described by the Landau-Lifshitz-Gilbert equation [7,8]:

$$\frac{1}{\gamma} \frac{dm}{dt} = m \times H_{\text{eff}} - \frac{\lambda}{\gamma_m} m \times \frac{dm}{dt} \dots \quad \dots \quad \dots \quad \dots \quad \dots \quad \dots \quad \dots \quad (2.3)$$

Where, γ is gyromagnetic ratio, m is magnetic moment, λ is damping coefficient and H_{eff} is effective magnetic field (the external field plus any self-field). The first term describes precession of the moment about the effective field, while the second is a damping term related to dissipation of energy caused by interaction with the surroundings.

2.1.4.2 Magnetic Moment of an Electron

Electrons and many elementary particles also have intrinsic magnetic moments, an explanation of which requires a quantum mechanical treatment and relates to the intrinsic angular momentum of the particles as discussed in the article Electron magnetic moment. It is these intrinsic magnetic moments that give rise to the macroscopic effects of magnetism, and other phenomena, such as resonance. The magnetic moment of the electron is,

$$m_s = -\frac{g_s\mu_B S}{\hbar} \dots \quad \dots \quad \dots \quad \dots \quad \dots \quad \dots \quad \dots \quad \dots \quad (2.4)$$

Where, μ_B is the Bohr magneton, S is electron spin, and the g -factor g_s is 2 according to Dirac's theory, but due to quantum electrodynamic effects it is slightly larger in reality: 2.002 319 304 36. The deviation from 2 is known as the anomalous magnetic dipole

moment. Again it is important to notice that m is a negative constant multiplied by the spin, so the magnetic moment of the electron is antiparallel to the spin. This can be understood with the following classical picture: if we imagine that the spin angular momentum is created by the electron mass spinning around some axis, the electric current that this rotation creates circulates in the opposite direction, because of the negative charge of the electron; such current loops produce a magnetic moment which is antiparallel to the spin. Hence, for a positron (the anti-particle of the electron) the magnetic moment is parallel to its spin.

2.1.5 The Hysteresis Loop

The hallmark of a magnetic system is the hysteresis loop. This is traditionally represented graphically as the overall magnetization of the sample against some applied magnetic field. The value of the applied field where the loop crosses zero magnetization is known as the coercive field H_c or B_c , and this therefore represents the amount of applied field required to reverse the magnetization direction of the magnet. The remanent magnetization M_r is the magnetization which remains when the applied field is reduced to zero. H_c or B_c The coercive field i.e. the applied field where the overall magnetization of a sample is zero. Comparing the hysteresis loops, such as those in figure 2.2, of a soft and a hard magnet, one can make the observation that the softer magnet will have a narrow hysteresis loop [9], i.e. the applied field necessary to reverse the magnetization is relatively low, and the hard magnet will possess a comparatively wide hysteresis loop.

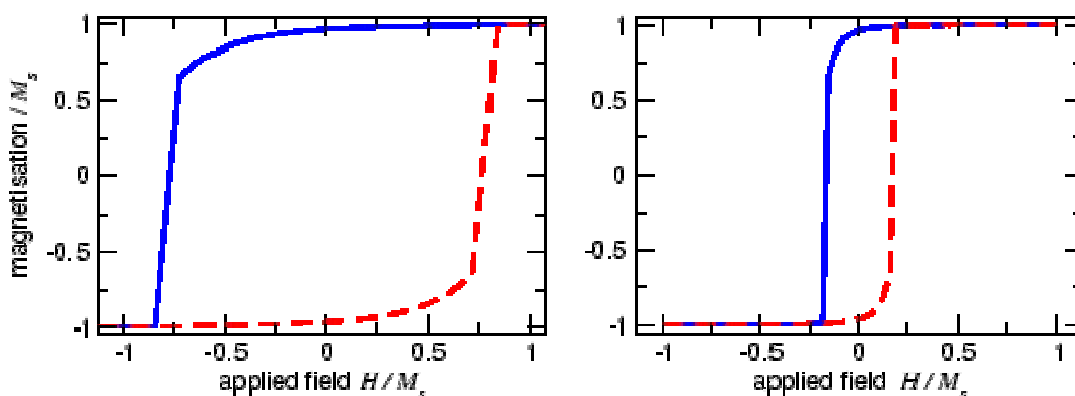


Figure 2.2: Two typical hysteresis loops - the left loop shows some permanently magnetic material, the right loop a softer magnet. The solid blue line indicates reducing field, the dashed red line indicates increasing field.

The point at which the overall magnetization of a sample can no longer be increased (as all the magnetization is pointing utterly in a single direction) is called the saturation point or M_s , which is identified as a plateau at the extremes of applied field in a hysteresis loop. Also one should note that the area underneath the hysteresis loop is equivalent to the energy which, when the field is reversed, is converted into heat.

For the long-term storage of data, it is desirable to have a material with a wide hysteresis loop, and therefore a large coercive field, as this makes it more difficult for the said material to lose its magnetization state. A narrow hysteresis loop is a characteristic beneficial for applications such as recording heads, as in these temporary magnetization promotes easy switching between magnetization states.

2.1.6 Magnetic Domains

A magnetic domain is a region within a magnetic material in which the magnetization is in a uniform direction. This means that the individual magnetic moments of the atoms are aligned with one another and they point in the same direction. When cooled below a temperature called the Curie temperature, the magnetization of a piece of ferromagnetic material spontaneously divides into many small regions called magnetic domains. The magnetization within each domain points in a uniform direction, but the magnetization of different domains may point in different directions. Magnetic domain structure is responsible for the magnetic behavior of ferromagnetic materials like iron, nickel, cobalt and their alloys, and ferrimagnetic materials like ferrite.

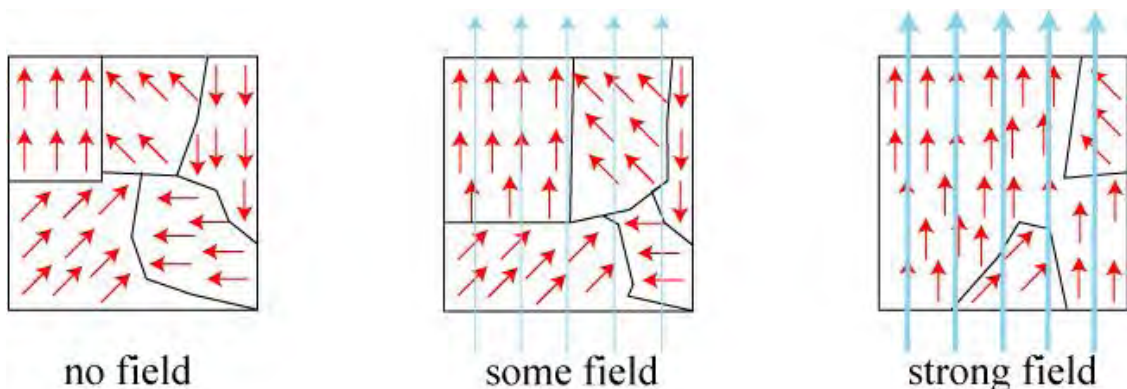


Figure 2.3: Illustration of domains in magnetic materials.

This includes the formation of permanent magnets and the attraction of ferromagnetic materials to a magnetic field. The regions separating magnetic domains are called domain walls, where the magnetization rotates coherently from the direction in one domain to that in the next domain. The study of magnetic domains is called micromagnetics.

2.1.7 Curie's Law

The susceptibilities of a number of paramagnetic solids were measured over a wide temperature range by Curie [10]. In this he found that the susceptibility varied inversely with temperature.

$$\chi = \frac{C}{T} \quad \dots \quad \dots \quad \dots \quad \dots \quad \dots \quad \dots \quad \dots \quad (2.5)$$

Where, C is a constant known as the Curie constant. The materials which obey this law are materials in which the magnetic moments are localized at the atomic or ionic sites. This can be considered to be 'dilute' magnetic materials, in which the magnetic atoms are surrounded by a number of non-magnetic atoms. Hydrated salts of transition metals such as $\text{CuSO}_4 \cdot 5\text{H}_2\text{O}$ and $\text{CrK}(\text{SO}_4) \cdot 12\text{H}_2\text{O}$ obey the Curie law.

2.1.8 Curie-Weiss Law

It was found that the susceptibilities of a number of paramagnetic metals obey a modified or generalized law known as the Curie- Weiss law [11]. In metals such as nickel and the lanthanides it was found to vary, which can be represented at least in the paramagnetic region by an equation of the form,

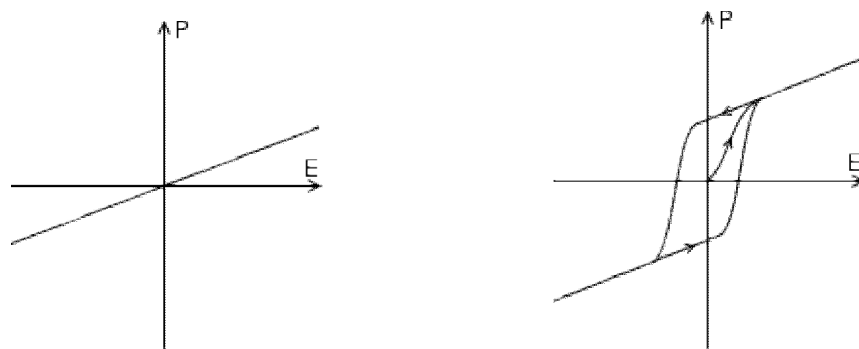
$$\chi = \frac{C}{T - T_C} \quad \dots \quad \dots \quad \dots \quad \dots \quad \dots \quad \dots \quad \dots \quad (2.6)$$

Where, C is again the Curie constant and T_C is another constant with dimensions of temperature. T_C can be either positive or zero. $T_C = 0$ corresponds of course to the earlier Curie law. For materials that undergo a paramagnetic to ferromagnetic transition $T_C > 0$ corresponds to the Curie temperature. For materials that undergo a paramagnetic to antiferromagnetic transition the term T_C is less than zero, although in practice the transition temperature between the paramagnetic and antiferromagnetic phases occurs at a positive temperature T_N known as the Neel temperature. It should be remembered that the susceptibility only follows the Curie- Weiss law in the paramagnetic region. Once the

material becomes ordered the susceptibility behaves in a very complicated way and no longer has a unique value for a given field strength.

2.2 Ferroelectricity

A ferroelectric material has a permanent electric dipole, and is named in analogy to a ferromagnetic material (e.g. Fe) that has a permanent magnetic dipole [12]. Ferroelectric materials exhibit a wide spectrum of functional properties, including switchable polarization, piezoelectricity, high non-linear optical activity, pyroelectricity, and non-linear dielectric behaviour. These properties are crucial for application in electronic devices such as sensors, microactuators, infrared detectors, microwave phase filters and, non-volatile memories [13]. This unique combination of properties of ferroelectric materials has attracted researchers and engineers for a long time. Ferroelectricity is a property of certain materials in which they possess a spontaneous electric polarization that can be reversed by the application of an external electric field. At null electric field, the material processes two or more discrete stable or metastable states with different nonzero electric polarization, but any two of states are identical in crystal structure. With the electric field, the polarization must be possible to switch between these states [14] [15]. The ferroelectricity is a subgroup of piezoelectricity which is a subgroup pyroelectricity.



(a) PE State

(b) FE State

Figure 2.4: P-E Relationships.

Thus, ferroelectric (FE) material has both pyroelectric and piezoelectric properties. The FE can be directly proved by FE hysteresis loop. The normal dielectric or the paraelectric (PE) state of FE has linear relationship between polarization and electric field (figure 2.4(a)) but the FE state has nonlinear hysteresis behavior (figure 2.4(b)). Importantly, the polarization (so-called spontaneous polarization) is not zero in the absent of an electric field and there are two polarization states. In contrast to FE, AFE are those in which some ferroic entities are spontaneously polarized along one direction while the adjacent ferroic groups are polarized in the opposite direction. Therefore, there is no net spontaneous polarization contrary to FE [16].

2.2.1 Classification of Ferroelectrics

Ferroelectric materials can be classified on the basis of their chemical composition and structure as:

(a) Rochelle salt: The first solid to show ferroelectric properties is Rochelle salt. Rochelle salt is the sodium-potassium salt of tartaric acid ($\text{NaKC}_4\text{H}_4\text{O}_6 \cdot 4\text{H}_2\text{O}$). It has the property of being ferroelectric only in the temperature range between -18°C and 23°C , which means it has two transition temperatures.

(b) Dihydrogen phosphates and arsenates: Busch and Scherier discovered ferroelectric properties in KH_2PO_4 in 1935 which is an example of the dihydrogen phosphate and arsenate of the alkali metals. The spontaneous polarization of this material a function of temperature. In contrast with Rochelle salt, KH_2PO_4 has one Curie temperature, $T_c = 123\text{K}$. Above the transition temperature it has a tetragonal structure and below T_c it is orthorhombic.

(c) Oxygen Octahedron group (Barium Titanate): The best known ferroelectric material is barium titanate (BaTiO_3) and it is a representative of the oxygen octahedron group of ferroelectric material. The reason for this name is that the above the Curie temperature that is at 120°C , BaTiO_3 corresponds to the cubic structure. When the temperature is decreased through the critical temperature of 120°C , the material becomes spontaneously polarized and at the same time the structure changes. BaTiO_3 has two more transition temperatures; one at 5°C , and other at -80°C . There will be a change in the crystal structure of the material associated with their ferroelectric transitions [17].

2.2.2 Perovskite

The mineral perovskite (CaTiO_3) was firstly discovered and named by Gustav Rose in 1839. Now, many compounds of ABO_3 composition are named perovskite. A / B represents a cation or mixture with different cations or/and vacancies, O represents O^{2-} . The function properties of perovskite oxides vary depending on composition and structure.

2.2.2.1 Structure and Properties of Perovskite

The perovskite structure with molecular formula ABO_3 may be visualized as a simple cubic lattice of an alkaline earth or lanthanide (A), with a transition metal (B) at the center of the unit cell surrounded by anions at the face centers. In figure 2.5 A is the larger cation and B is the smaller cation. In this structure, the B cation is 6-fold coordinated and the A cation is 12-fold coordinated with the oxygen anions.

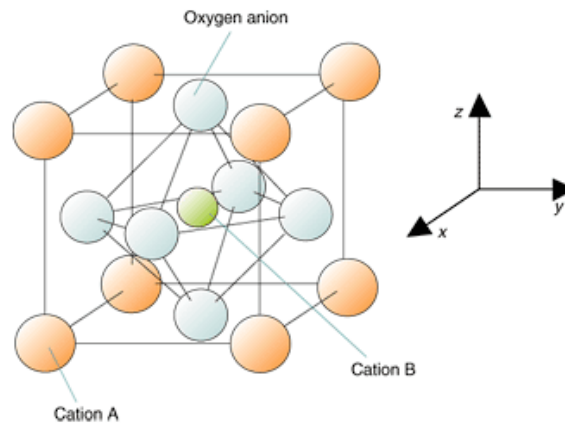


Figure 2.5: Schematic illustration of the ABO_3 perovskite structure.

In ideal perovskite, where the atoms are touching one another, the B - O distance is $a/2$ (a is the cubic unit cell parameter) while A - O distance is $a/\sqrt{2}$ and the following relationship between ionic radii holds: $r_A + r_O = \sqrt{2}(r_B + r_O)$. However, it was found that the cubic structure was still retained in ABO_3 compounds, even though this equation is

not exactly obeyed. As a measure of the deviation from the ideal situation, tolerance factor (t), is defined by the following equation,

$$t = \frac{r_A + r_O}{\sqrt{2}(r_B + r_O)} \quad \dots \quad \dots \quad \dots \quad \dots \quad \dots \quad \dots \quad (2.7)$$

Which, is applicable at room temperature to the empirical ionic radii. Here, r_A is the average ionic radius of the A site atoms, r_B is the average ionic radius of B site atoms and r_O is the ionic radius of O^{2-} . For ideal perovskite, the value of t is equal to 1 and for distorted perovskite, this value should be less than or more than 1. The ideal perovskite structure appears in a few cases for t -values very close to 1 and at high temperatures. In the most cases, different distortions of the perovskite structure appear.

2.2.2.2 The Deformation of Perovskite

Many function properties are directly related to deformation of perovskite. The deformation was first studied by H. D. Megaw [18,19], A. M. Glazer [20,21] and else. It can be classified into three types:

1. Cation Displacement,
2. Octahedron Distortion,
3. Anion Octahedron Tilt.

Cation displacement is found in many compounds, especially in ferroelectric materials. Octahedron distortion occurs in magnetic perovskites. Tilt is a more complex deformation which reflects the rotation of neighbouring octahedrons.

2.3 Dielectrics

A dielectric material is an electrical insulator that can be polarized by an applied electric field. When a dielectric is placed in an electric field, electric charges do not flow through the material as they do in a conductor, but only slightly shift from their average equilibrium positions causing dielectric polarization. Because of dielectric polarization, positive charges are displaced toward the field and negative charges shift in the opposite direction [22]. This creates an internal electric field that reduces the overall field within the dielectric itself. If a dielectric is composed of weakly bonded molecules, those molecules not only become polarized, but also reorient so that their symmetry axes align to the field.

2.3.1 Dielectric Polarization

Dielectric polarization occurs when a dipole moment is formed in an insulating material because of an externally applied electric field. When a current interacts with a dielectric material, the dielectric material will respond with a shift in charge distribution with the positive charges aligning with the electric field and the negative charges aligning against it [23]. A simple picture can be made using a capacitor as an example. The figure below (figure 2.6) shows an example of a dielectric material in between two conducting parallel plates. The charges in the material will have a response to the electric field caused by the plates.

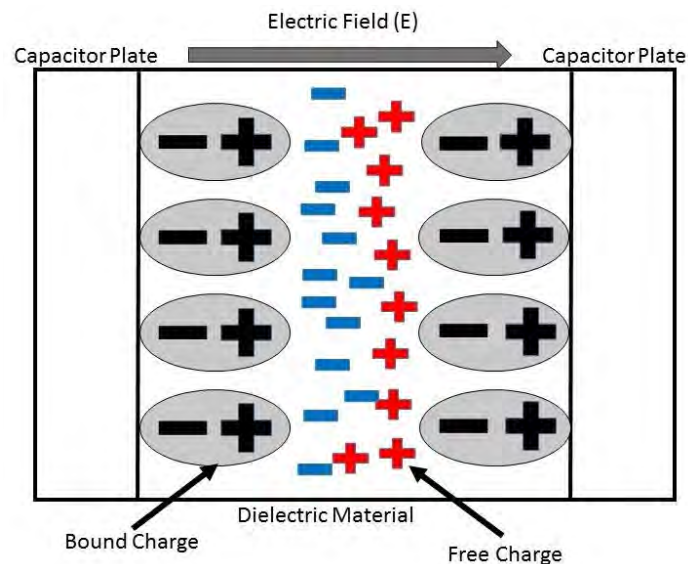


Figure 2.6: The bound charges are the charges that are touching the capacitor plates, while the free charges usually float around in the material, but for this case, they are aligned with the bound charges.

Using the capacitor model, it is possible to define the relative permittivity or the dielectric constant of the material by setting its relative permittivity equivalent to the ratio of the measured capacitance and the capacitance of a test capacitor, which is also equal to the absolute permittivity of the material divided by the permittivity of vacuum.

The dielectric constant is an important term, because another term known as the electronic polarizability can be related to the dielectric constant. The electronic polarizability is a microscopic polarization phenomena that occurs in all materials and is one of the main mechanisms that drives dielectric polarization [24]. To explain how the dielectric constant relates to the electronic polarizability of a material, the polarization

($p = qd$) of a material should be determined. The polarization of a material is defined as the total dipole moment per unit volume. The type of polarization on a microscopic scale is determined by the material. Most materials exhibit polarization only in the presence of an external field. A few (e.g. ferroelectric materials) however show permanent polarization. The four types of polarization which occur in dielectrics are:

- (a) Electronic Polarization
- (b) Ionic Polarization
- (c) Orientation or Dipole Polarization
- (d) Interfacial or Space charge Polarization

Electronic polarization: Electronic polarization occurs due to displacement of the centre of the negatively charged electron cloud relative to the positive nucleus of an atom by the electric field. Mono-atomic gases exhibit only electronic polarization. The shifting of electron cloud results in dipole moment and dipole moment p is defined as the product of the charge and shift distance, that is $p = qd$. Dipole moment p is also directly proportional to electric field strength, E thus p is proportional to E Or $p = \alpha_e E$, where α_e is constant of proportionality known as electronic polarizability constant. Electronic polarization P_e is given as $P_e = np$ where n is number of molecules per unit volume. Therefore, electronic polarization can be written as $P_e = n\alpha_e E$; This polarization is independent of temperature.

Ionic Polarization: Ionic polarization is a mechanism that contributes to the relative permittivity of a material. This type of polarization typically occurs in ionic crystal elements such as NaCl, KCl, and LiBr.

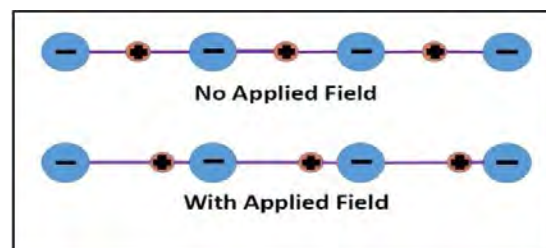


Figure 2.7: The effect of an external electric field on an ionic material. The positive charges will flow with the field and the negative charges will flow against the field, causing a net average dipole moment per ion to form.

There is no net polarization inside these materials in the absence of an external electric field because the dipole moments of the negative ions are canceled out with the positive ions. However, when an external field is applied, the ions become displaced, which leads to an induced polarization. Figure 2.7 shows the displacement of ions due to this external electric field. Usually the ionic polarizability is greater than the electronic polarizability by a factor of 10 which leads to ionic substances having high dielectric constants. Similar to electronic polarization, ionic polarization also has a total polarization associated with it.

Orientation or Dipole Polarization: Orientational polarization arises when there is a permanent dipole moment in the material. Materials such as HCl and H₂O will have a net permanent dipole moment because the charge distributions of these molecules are skewed. For example, in a HCl molecule, the chlorine atom will be negatively charged and the hydrogen atoms will be positively charged causing the molecule to be dipolar. The dipolar nature of the molecule should cause a dipole moment in the material, however, in the absence of an electric field, the dipole moment is canceled out by thermal agitation resulting in a net zero dipole moment per molecule. When an electric field is applied however, the molecule will begin to rotate to align the molecule with the field, causing a net average dipole moment per molecule.

Interfacial or Space charge Polarization: Interfacial or space charge polarization occurs when there is an accumulation of charge at an interface between two materials or between two regions within a material because of an external field. This can occur when there is a compound dielectric, or when there are two electrodes connected to a dielectric material. This type of electric polarization is different from orientational and ionic polarization because instead of affecting bound positive and negative charges i.e. ionic and covalent bonded structures, interfacial polarization also affects free charges as well. As a result interfacial polarization is usually observed in amorphous or polycrystalline solids. Figure 2.8 shows an example of how free charges can accumulate in a field, causing interfacial polarization. The electric field will cause a charge imbalance because of the dielectric material's insulating properties. However, the mobile charges in the dielectric will migrate over maintain charge neutrality. This then causes interfacial polarization.

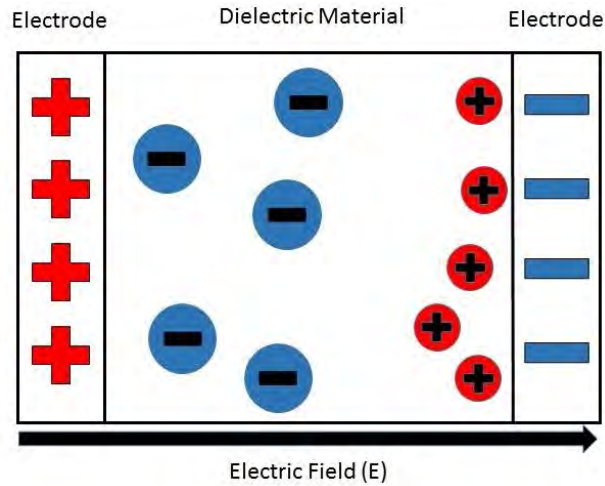


Figure 2.8: This shows how the free positive charges inside the dielectric material migrate towards the negative charge build-up on the right, caused by the external electric field.

2.3.2 Dielectric Constant

Dielectric constant is the property of an electrical insulating material (a dielectric) equal to the ratio of the capacitance of a capacitor filled with the given material to the capacitance of an identical capacitor in a vacuum without the dielectric material. The insertion of a dielectric between the plates of, say, a parallel-plate capacitor always increases its capacitance, or ability to store opposite charges on each plate, compared with this ability when the plates are separated by a vacuum. If C is the value of the capacitance of a capacitor filled with a given dielectric and C_0 is the capacitance of an identical capacitor in a vacuum, the dielectric constant, symbolized by the Greek letter kappa, κ , is simply expressed as $\kappa = C/C_0$. E is always less than or equal to E_0 , so the dielectric constant is greater than or equal to 1. The larger the dielectric constant, the more charge can be stored. Completely filling the space between capacitor plates with a dielectric increases the capacitance by a factor of the dielectric constant: $C = \kappa C_0$, where, C_0 is the capacitance with no dielectric between the plates. For a parallel plate capacitor containing a dielectric that completely fills the space between the plates, the capacitance is given by:

$$C = \frac{\kappa \epsilon_0 A}{d} \dots \dots \dots \dots \dots \dots \dots \dots \dots \dots (2.8)$$

This is the only variable left with the material scientist to increase the capacitance per unit volume of capacitor for modern electronics application.

2.3.3 Dielectric Loss

Dielectric loss is the loss of energy that goes into heating a dielectric material in a varying electric field. For example, a capacitor incorporated in an alternating-current circuit is alternately charged and discharged each half cycle. During the alternation of polarity of the plates, the charges must be displaced through the dielectric first in one direction and then in the other, and overcoming the opposition that they encounter leads to a production of heat through dielectric loss, a characteristic that must be considered when applying capacitors to electric circuits. Dielectric loss quantifies a dielectric material's inherent dissipation of electromagnetic energy into, e.g. heat. It can be parameterized in terms of either the loss angle δ or the corresponding loss tangent $\tan\delta$. In such electromagnetic analysis, the parameters permittivity ϵ , permeability μ , and conductivity σ represent the properties of the media through which the waves propagate. The permittivity can have real and imaginary components (the latter excluding σ effects, see below) such that,

$$\epsilon = \epsilon' - j\epsilon'' \dots \dots \dots (2.9)$$

If we assume that we have a wave function such that,

$$E = E_0 e^{j\omega t} \dots \dots \dots (2.10)$$

Then, Maxwell's curl equation for the magnetic field can be written as,

$$\Delta \times H = j\omega \epsilon' E + (\omega \epsilon'' + \sigma) E \dots \dots \dots (2.11)$$

Where, ϵ'' is the imaginary component of permittivity attributed to bound charge and dipole relaxation phenomena, which gives rise to energy loss that is indistinguishable from the loss due to the free charge conduction that is quantified by σ . The component ϵ' represents the familiar lossless permittivity given by the product of the free space permittivity and the relative real permittivity, or $\epsilon' = \epsilon_0 \epsilon'_r$. The loss tangent is then defined as the ratio (or angle in a complex plane) of the loss reaction to the electric field E in the curl equation to the lossless reaction:

$$\tan\delta = \frac{\omega\epsilon'' + \sigma}{\omega\epsilon'} \dots \dots \dots (2.12)$$

For dielectrics with small loss, this angle is $\ll 1$ and $\tan \delta \approx \delta$. After some further maths to obtain the solution for the fields of the electromagnetic wave, it turns out that the power decays with propagation distance z as,

$$P = P_0 e^{-\delta k z}, \quad \dots \dots \dots (2.13)$$

$$k = \omega \sqrt{\mu \epsilon'} = \frac{2\pi}{\lambda} \dots \dots \dots (2.14)$$

where, P_0 is the initial power, ω is the angular frequency of the wave, and λ is the wavelength in the dielectric. There are often other contributions to power loss for electromagnetic waves that are not included in this expression, such as due to the wall currents of the conductors of a transmission line or waveguide. Also, a similar analysis could be applied to the permeability where,

$$\mu = \mu' - j\mu'' \dots \dots \dots (2.15)$$

With the subsequent definition of a magnetic loss tangent

$$\tan \delta_m = \frac{\mu''}{\mu'} \dots \dots \dots (2.16)$$

The electric loss tangent can be similarly defined:

$$\tan \delta_e = \frac{\epsilon''}{\epsilon'} \dots \dots \dots (2.17)$$

2.3.4 Dependence of Dielectric Constant on Frequency

Electrons have very much smaller mass than that of ions, so they respond more rapidly to a changing electric field. For electric field that oscillates at extremely high frequencies (like light) only electronic polarization can take place. At lesser frequencies, the relative displacement of positive and negative ions can take place. Orientation of permanent dipoles, which require the rotation of a molecule can occur only if the oscillation is relatively slow (MHz range or slower). The total polarization P , total polarizability and the relative permittivity of a dielectric in an alternating field all depend on the ease with which the dipoles can reverse alignment with each other reversal of the field. Some polarizability mechanisms do not permit sufficiently rapid reversal of the dipole alignment. In such a process the time required to reach the equilibrium orientation is

called the relaxation time and its reciprocal the relaxation frequency. It can be also defined as the time specific polarization to occur is called the relaxation time. When the frequency of the applied field exceeds that of the relaxation frequency of a particular polarization process, the dipoles cannot reorient fast enough and operation of the process ceases.

2.4 Magnetoelectric Effect

The magnetoelectric effect was first conjectured by P. Curie [25] in 1894 while the term "magnetoelectric" was coined by P. Debye [26] in 1926. A more rigorous prediction of a linear coupling between electric polarization and magnetization was shortly formulated by L.D. Landau and E. Lifshitz in one book of their famous series on theoretical physics [27]. Only in 1959, I. Dzyaloshinskii [28], using an elegant symmetry argument, derived the form of a linear magnetoelectric coupling in Cr_2O_3 . The experimental confirmation came just few months later when the effect was observed for the first time by D. Astrov [29]. The general excitement which followed the measurement of the linear magnetoelectric effect leads to the organization of the series of MEIPIC (Magnetoelectric Interaction Phenomena in Crystals) conferences. Between the prediction of I. Dzialoshinskii and the MEIPIC first edition (1973) more than 80 linear magnetoelectric compounds were found. Recently, technological and theoretical progress triggered a renaissance of these studies and magnetoelectric effect is still heavily investigated. The magnetoelectric (ME) effect is the phenomenon of inducing magnetic (electric) polarization by applying an external electric (magnetic) field. The effects can be linear or/and non-linear with respect to the external fields. In general, this effect depends on temperature. The effect can be expressed in the following form,

$$P_i = \sum \alpha_{ij} H_j + \sum \beta_{ijk} H_i H_k + \dots \dots \dots \dots \quad (2.18)$$

$$M_i = \sum \alpha_{ij} E_j + \sum \beta_{ijk} E_i E_k + \dots \dots \dots \dots \quad (2.19)$$

Where, P is the electric polarization, M the magnetization, E and H the electric and magnetic field, and α and β are the linear and nonlinear ME susceptibilities. The effect can be observed in single phase and composite materials. Some examples of single phase magnetoelectrics are Cr_2O_3 [30], and multiferroics materials which show a coupling

between the magnetic and electric order parameters. Composite magnetoelectrics are combinations of magnetostrictive and electrostrictive materials, such as ferromagnetic and piezoelectric materials. The size of the effect depends on the microscopic mechanism. In single phase magnetoelectrics the effect can be due to the coupling of magnetic and electric orders as observed in some multiferroics. In composite materials the effect originates from interface coupling effects, such as strain. Some of the promising applications of the ME effect are sensitive detection of magnetic fields, advanced logic devices and tunable microwave filters [30].

2.5 Multiferroics

The simultaneous coexistence of at least two ferroic properties, (anti)ferromagnetism, (anti) ferroelectricity and (anti)ferroelasticity in the same phase is defined as multiferroics, as shown in figure 2.9. These materials have the potential of exhibiting coupling between ferroelectricity and magnetism, known as the magnetoelectric effect, which enables the external electric field to change magnetization and vice versa [31]. However, looking back in history, the combination and correlation of magnetism and electricity were well interpreted by Maxwell equations in the 19th century, but magnetic and electric ordering in solids were always treated separately at that time. This is because the magnetic properties were understood to be attributed to the spin of electrons while the electric properties resulted from the electric charges of ions and electrons. This situation changed after the hypothesis was proved to be untrue. The preliminary proposal of the magnetoelectric effect was made in 1894 by Curie indicating that an asymmetric molecular body can be polarized by a magnetic field. Later in 1960, Dzyaloshinskii [33] predicted the magnetoelectric effect in antiferromagnetic Cr_2O_3 and in the meantime, Astrov [10] also observed this coupling by measuring the electric field-induced magnetization. The magnetic field induced electric polarization was also studied by Folen et al. [11] in 1961. Now-a-days, the coexistence of ferroelectricity and magnetism attracts a great deal of attention. The potential application of multiferroics is quite extensive and promising, ranging from giant electric transformers to a small computer memory devices or even tiny sensors [34].

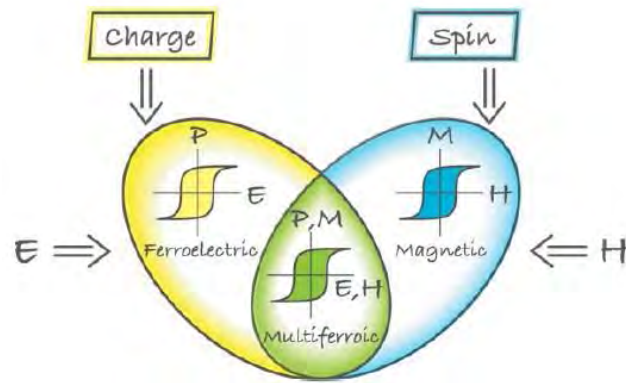


Figure 2.9: Multiferroics combine the properties of ferroelectrics and magnets (green). In the ideal case, the magnetization of a ferromagnet in a magnetic field displays the usual hysteresis (blue), and ferroelectrics have a similar response to an electric field (yellow) [32].

Unfortunately, most of the multiferroics are not naturally-occurring materials and fewer materials possess magnetoelectric properties. Majority of multiferroic materials have low magnetic ordering and ferroelectric transition temperature. This can be partly improved by introducing dopants (such as rare earth elements) into the original material. Moreover, since the microscopic origin of magnetism can be described as the presence of localized electrons, mainly in the partially filled d or f shell of transition metals or rare-earth ions having a corresponding localized spin. By contrast, ferroelectric materials require transition metal ion with an empty d shell, and the displacement of such transition metal ion towards an apical atom (normally oxygen) creates electric dipoles that are stabilized by the strong covalent bonds between O 2p and empty d orbitals. The mutual exclusion of ferroelectricity and magnetism give rise to a problem called " d^0 versus d^n ". In order for the coexistence of magnetism and ferroelectricity to occur, both the elements and structures need to be considered. In the perovskite type structure (ABO_3) multiferroics, the A site element is selected to take the responsibility for the ferroelectricity while the element at the B site accounts for the magnetism. For instance in the perovskite $BiMnO_3$, the $6s^2$ lone pair of Bi^{3+} tends to hybridize with O 2p orbital, which improves the ferroelectricity by driving the Bi^{3+} towards the oxygen ions, while the Mn cation has nonzero d-electrons.

2.5.1 Different Types of Multiferroics

The microscopic origin of magnetism is basically the same in all magnets: it is the presence of localized electrons, mostly in the partially filled d or f shells of transition

metal or rare-earth ions, which have a corresponding localized spin, or magnetic moment. Exchange interactions between the localized moments lead to magnetic order. The situation with ferroelectrics is quite different. There are several different microscopic sources of ferroelectricity, and accordingly one can have different types of multiferroics. Generally, there are two groups of multiferroics. The first group, which can be called type-I multiferroics, contains those materials in which ferroelectricity and magnetism have different sources and appear largely independently of one another, though there is some coupling between them. In these materials, ferroelectricity typically appears at higher temperatures than magnetism, and the spontaneous polarization P is often rather large (of order $10 - 100 \mu\text{C}/\text{cm}^2$). Examples are BiFeO_3 ($T_{\text{FE}} \sim 1100\text{K}$, $T_{\text{N}} = 643 \text{ K}$, $P \sim 90\mu\text{C}/\text{cm}^2$) and YMnO_3 ($T_{\text{FE}} \sim 914\text{K}$, $T_{\text{N}} = 76 \text{ K}$, $P \sim 6\mu\text{C}/\text{cm}^2$). The second group, which we can call type-II multiferroics, is the relatively recently discovered materials, in which magnetism causes ferroelectricity, implying a strong coupling between the two [32]. However, the polarization in these materials is usually much smaller ($\sim 10^{-2} \mu\text{C}/\text{cm}^2$). Many groups are also investigating composite multiferroics that consist of known magnets and ferroelectrics in the form of multilayers and selforganized nanostructures.

Type-I multiferroics: Type-I multiferroics are “older” and more numerous. These are often good ferroelectrics, and the critical temperatures of the magnetic and ferroelectric transitions can be well above room temperature. Unfortunately, the coupling between magnetism and ferroelectricity in these materials is usually rather weak. The materials challenge for this group of multiferroics is to keep all their positive features, but enhance this coupling. As we will see later, the opposite problem exists for type-II multiferroics. One can single out several different subclasses of type-I multiferroics, depending on the mechanism of ferroelectricity in them.

Type-II multiferroics (Magnetic multiferroics): The biggest excitement nowadays is caused by the discovery of a novel class of multiferroics in which ferroelectricity exists only in a magnetically ordered state and is caused by a particular type of magnetism. For example, in TbMnO_3 magnetic ordering appears at $T_{\text{N1}} = 41 \text{ K}$, and at a lower temperature, $T_{\text{N2}} = 28 \text{ K}$, the magnetic structure changes. It is only in the lowtemperature phase that a nonzero electric polarization appears. Similar behavior occurs in TbMn_2O_5 . The first paper to study TbMnO_3 showed that a magnetic field can strongly influence the

electric polarization: e.g., in TbMnO_3 the polarization rotates (or “flops”) by 90 degrees when a critical magnetic field is applied along a certain direction. In TbMn_2O_5 the influence of an external field is even stronger: the polarization changes sign with field, and a field alternating between +1.5 and -1.5 Tesla leads to corresponding oscillations in the polarization. Since the discovery of these materials, a number of other type-II multiferroics with strong magnetoelectric coupling have been discovered and studied. From the point of view of the mechanism of multiferroic behavior, one can divide type-II multiferroics into two groups: those in which ferroelectricity is caused by a particular type of magnetic spiral and those in which ferroelectricity appears even for collinear magnetic structures.

2.5.2 BiFeO_3 Multiferroic

Bismuth ferrite (BiFeO_3) is one of the few multiferroics that has Curie and Neel temperatures above room temperature. Magnetoelectric coupling is realized at room temperature and such coupling is strongly enhanced by proper dopings [35]. BiFeO_3 is a typical multiferroic material that has been extensively investigated nowadays. The initial research on BiFeO_3 was carried out by Smolenskii in 1960 [36]. But at that time, they were not able to make single phase polycrystalline BiFeO_3 and the BiFeO_3 produced was not stable for practical application. In 1967, Achenbach successfully prepared single phase BiFeO_3 by removing the undesirable phases using HNO_3 [37]. X-ray diffraction technique was also adopted to investigate the mono-domain single phase by Kubel and Schmid in 1990 [38]. Later in 2003, Ramesh and his colleagues produced thin film BiFeO_3 which exhibited remnant polarization 15 times stronger than that of the bulk BiFeO_3 [39]. It has also been reported that the low symmetry monoclinic or tetragonal thin film BiFeO_3 might be the origins of strong polarization [25,26]. Until recently, increasing efforts have also been devoted to the research focusing on the preparation and characterization of BiFeO_3 in forms of film, bulk and nanostructure [27,28].

Single phase BiFeO_3 has rhombohedrally distorted perovskite structure $R3c$ with antiphase rotation of FeO_6 octahedra by 12° , denoted as a-a-a- in the Glazer notation. The displacement of the A-site bismuth cation along the [111] pseudo-cubic axis brings about a non-centrosymmetric polarization resulting in the ferroelectric property. The lattice

parameters for bismuth ferrite with rhombohedral structure are 3.965\AA and 89.4° [29] or $a = 5.58\text{\AA}$ and $c = 13.9\text{\AA}$ if viewed in the hexagonal setting at room temperature [30]. The lattice parameter and crystal structure of BiFeO_3 are dependent on the temperature. It was well documented that, except for the long Bi-Fe bond distance, the lattice parameter a , c , the volume of unit cell, the short bond distance of Bi - Fe as well as the bond angles gradually increase with increase in temperature. As a consequence of these variations, magnetism and polarization are reported to be gradually reduced, and structural phase transitions are also induced from the rhombohedrally distorted $R3c$ perovskite structure to an orthorhombic $Pnma$ structure at 1098K and eventually to a cubic structure above 1204K [40]. However, single phase BiFeO_3 is difficult to synthesize. Due to the meta stable nature of bismuth ferrite in air [41] as well as the volatility of bismuth oxide, their stoichiometry can be changed resulting in impurities of Bi_2O_3 , $\text{Bi}_{25}\text{FeO}_{39}$ and Bi_2FeO_9 during the sintering process.

2.5.3 Recent Progress of Multiferroics

The history of magnetoelectric multiferroics can be traced back to the 1960s [42]. In the most general sense the field of multiferroics was born from studies of magnetoelectric systems. In recent 10 years, there is a great revival in multiferroics. In 2000, Nicola A. Hill gave an answer about scarcity of ferromagnetic ferroelectric coexistence [43]. In 2003 the large ferroelectric polarization was discovered in epitaxially grown thin films of BiFeO_3 [44]. The same year, the strong magnetic and electric coupling was found in orthorhombic TbMnO_3 [45] and TbMn_2O_5 [46]. The recent studies of multiferroics clearly show the important of collaboration between experiment technology and modeling design. There are many classic review articles discussing the interesting multiferroics [47-51].

Reference:

- [1] Chikazumi, "S. Physics of Magnetism", John Wiley and Sons, Ltd., 1984.
- [2] Clarke, J., "SQUIDS." Scientific American, 46-53, August, 1994.
- [3] Cox, D.L. and Maple, M. B., "Electronic Pairing in Exotic Superconductors", Physics Today, 32-40, 1995.
- [4] Tilley, RJD, "Understanding Solids", John Wiley and Sons. p. 368, ISBN 0-470-85275-5, 2004.
- [5] Paul Allen Tipler, Llewellyn, R. A., "Modern Physics (4 ed.)", Macmillan. p. 310, ISBN 0-7167-4345-0, 2002.
- [6] Crowther, J. A., "Ions, Electrons and Ionizing Radiations (reprinted Cambridge (1934) 6 ed.)", Rene Press. p. 277, ISBN 1-4067-2039-9, 2007.
- [7] Stuart Alan Rice, "Advances in chemical physics", Wiley. pp. 208 ff, ISBN 0-471-44528-2, 2004.
- [8] Marcus Steiner, "Micromagnetism and Electrical Resistance of Ferromagnetic Electrodes for Spin Injection Devices", CuvillierVerlag. p. 6, ISBN 3-86537-176-0, 2004.
- [9] Afremov, L. L. and Panov, A. V., "Magnetic states and hysteresis properties of small magnetite particles", Physics of Metals and Metallography, 86(3), 269-275, 1998.
- [10] Astrov, D. N., "Themagnetolectric effect in antiferromagnetics", Sov. Phys. JETP 11, 708-709, 1960.
- [11] Folen et al., V. J., "Anisotropy of the magnetolectric effect in Cr₂O₃", Phys. Rev. Lett. 6, 607-608, 1961.
- [12] Littlewood, P. B., " Physics of Ferroelectrics", January 27, 2002.
- [13] Indrani Coondoo, "Ferroelectrics", In Tech, pages 464, December 14, 2010.
- [14] Lines, M.E. and Glass, A.M, " Principles and Applications of Ferroelectrics and Related Materials", Clarendon Press, Oxford, PP 680, 1977.
- [15] Karin M., Rabe, Charles H., Ahn, and Jean-Marc Triscone (editors), " Physics of Ferroelectrics", volume 105 of Topics in Applied Physics. Springer-Verlag Berlin Heidelberg, PP 19, 2007.

- [16] Kittel, C., “Theory of antiferroelectric crystals”, *Phys. Rev.*, 82(5), pp 729–732, June 1951.
- [17] Siva, “Electromagnetism: Classification of ferroelectric materials”, *Winner Science*, 2011.
- [18] Megaw, H., “Origin of ferroelectricity in barium titanate and other perovskite-type crystals”, *Acta Crystallographica*, 5(6), pp 739–749, 1952.
- [19] Megaw, H.D. and Darlington, C.N.W., “Geometrical and structural relations in the rhombohedral Perovskites”, *Acta Crystallographica Section A*, 31(2), pp 161–173, Mar 1975.
- [20] Glazer, A., “The classification of tilted octahedra in perovskites”, *Acta Crystallographica Section B*, 28(11), pp 3384–3392, 1972.
- [21] Glazer, A., “Simple ways of determining perovskite structures”, *Acta Crystallographica Section A*, 31(6), pp 756–762, 1975.
- [22] Bunget, I., & Popescu, M., “Physics of solid dielectrics”, Amsterdam: Elsevier, 1984.
- [23] Kao, K., “Dielectric phenomena in solids with emphasis on physical concepts of electronic processes”, Amsterdam: Academic Press, 2004.
- [24] Kasap, S., “Principles of electronic materials and devices (3rd ed.)”, Boston: McGraw-Hill, 2006.
- [25] Curie, p., “Les conditions de symétrie nous permettent d’imaginer qu’un corps à molécule dissymétrique se polarise peut-être magnétiquement lorsqu’on le place dans un champ électrique.”, *J. Physique*, 3i^{ème} s’erie III, 393, 1894.
- [26] Debye, P., “Bemerkung zu einigen neuen Versuchen über einen magneto-elektrischen Richteffekt”, *Z. Phys.* 36, 300, 1926.
- [27] Landau, L. D., & Lifshitz, E. M., “Electrodynamics of continuous media” Pergamon, Oxford press, 1960.
- [28] Dzyaloshinskii, I.E., “On the magneto-electrical effect in antiferromagnetics”, *Zh. Exp. Teor. Fiz.* 37, 881, 1960.
- [29] Astrov, D., “Dynamical magnetoelectric effects in multiferroic oxides”, *Sov. Phys. JETP* 11, 708, 1960.

- [30] Nan, C. W., et al., “Multiferroic magnetoelectric composites: Historical perspective, status, and future directions”, *J. App. Phys.* 103, 031101, 2008.
- [31] Cai, Shengzhen, “Bismuth-containing multiferroics Synthesis, structure and magnetic properties”, Chalmers, Gothenburg, Sweden, 2013.
- [32] Daniel Khomskii, “Classifying multiferroics: Mechanisms and effect”, *Physics* 2, 20, 2009.
- [33] Dzyaloshinskii, I.E., “On the magneto-electrical effect in antiferromagnets”, *Sov. Phys. JETP* 10, 628, 1960.
- [34] Hans Schmid, “MultiferroicMagnetoelectrics”, *Ferroelectrics* 162, 317-338, 1994.
- [35] Litvin, D.B., “Ferroic classifications extended to ferrotoroidiccrystals” *Acta Cryst.*, A64, 316-320, 2008.
- [36] Heron, J. T., et al., “Electric-field-induced magnetization reversal in a ferromagnet-multiferroic heterostructure”, *Phys. Rev. Lett.* 107, 217202, 2011.
- [37] Seidel, J., et al., “Conduction at domain walls in oxide multiferroics”, *Nature Materials* 8, 229-234, 2009.
- [38] Hoffmann, T., et al., “Time-resolved imaging of magnetoelectric switching in multiferroic $MnWO_4$ ”, *Phys. Rev. B* 84, 184404, 2011.
- [39] Salje, E. K. H., “Multiferroic domain boundaries as active memory devices: Trajectories towards domain boundary engineering”, *Chem. Phys. Chem.* 11, 940-950, 2010.
- [40] Van Run, A. M., Terrell, D. R. and Scholing, J. H., “ An site Grown Eutectic Magnetoelectric Composite Material Part 2 Physical Properties, *J. of mat. Sci.*, Vol-9, pp 1710-1714, 1974.
- [41] Mazumder, S. and Bhattacharyya, G. S., “ Synthesis and Characterization of In Situ Grown Magnetoelectric Composites in the BaO-TiO-FeO-CoO System”, *Cera. Int.*, Vol-30, pp 389-392, 2004.
- [42] Ascher, E., Rieder, H., Schmid, H., and Stössel, H., “Some properties of ferromagnetoelectric nickel iodine boracite, $Ni_3B_7 O_{13}I$ ”, *Journal of Applied Physics*, 37(3):1404–1405, 1966.

- [43] Nicola, A., Hill. “Why are there so few magnetic ferroelectrics?”, *The Journal of Physical Chemistry B*, 104(29):6694–6709, July 2000.
- [44] Wang, J., Neaton, J. B., Zheng, H., Nagarajan, V., Ogale, S. B., Liu, B., Viehland, D., Vaithyanathan, V., Schlom, D. G., Waghmare, U. V., Spaldin, N. A., Rabe, K. M., Wuttig, M., and Ramesh, R.,” Epitaxial BiFeO₃ multiferroic thin film heterostructures”, *Science*, 299(5613):1719 –1722, March 2003.
- [45] Kimura, T., Goto, T., Shintani, H., Ishizaka, K., Arima, T., and Tokura, Y, “Magnetic control of ferroelectric polarization”, *Nature*, 426(6962):55–58, November 2003.
- [46] Hur, N., Park, S., Sharma, P. A., Ahn, J. S., Guha, S., and Cheong, S. W., “Electric polarization reversal and memory in a multiferroic material induced by magnetic fields”, *Nature*, 429(6990):392–395, May 2004.
- [47] Manfred Fiebig, “Revival of the magnetoelectric effect”, *Journal of Physics D: Applied Physics*, 38(8):R123, 2005.
- [48] Eerenstein, W., Mathur, N. D., and Scott, J. F., “Multiferroic and magnetoelectric materials”, *Nature*, 442(7104):759–765, 2006.
- [49] Sang-Wook Cheong and Maxim Mostovoy, “Multiferroics: a magnetic twist for ferroelectricity”, *Nat Mater*, 6(1):13–20, January 2007.
- [50] Daniel Khomskii, “Classifying multiferroics: Mechanisms and effects”, *Physics*, 2, 20, Mar 2009.
- [51] Wang, K. F., Liu, J. M., and Ren, Z. F., “Multiferroicity: the coupling between magnetic and polarization orders”, *Advances in Physics*, 58(4):321–448, 2009.

Chapter 3

Experimental Details

3.1 Sample Preparation

The bulk polycrystalline samples having compositions $\text{Bi}_{10.9}\text{Gd}_{0.1}\text{Fe}_{1-x}\text{Ti}_x\text{O}_3$ ($x = 0.00 - 0.25$) were synthesized by solid state reaction technique. Detail steps of this technique are described below.

3.1.1 Solid State Reaction Technique

There exist a wide variety of methods for the synthesis of polycrystalline materials. Out of them, the solid state reaction method is the broadly used technique for the preparation of polycrystalline solids.

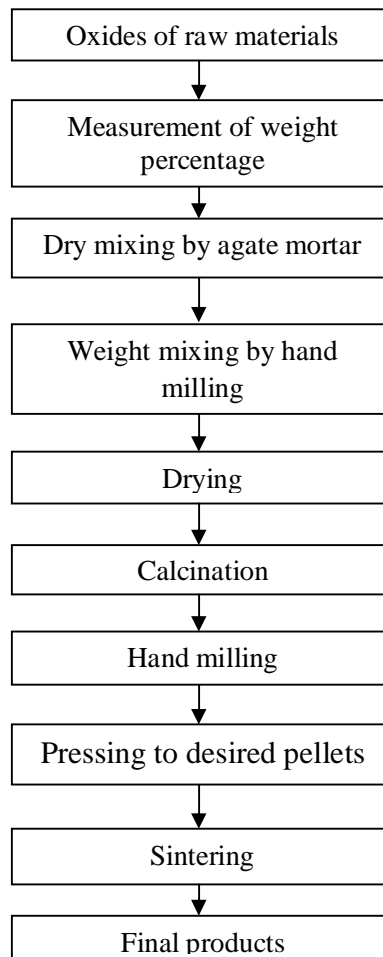


Figure 3.1: Flow chart of solid state reaction technique.

In this method reactants are mixed together in a powder form and heated for extended periods at high temperature. High temperature provides a considerable amount of energy to accelerate the reaction rate. Hence, the final product obtained from this method is thermodynamically stable. The major benefit of this method is the formation of structurally single phase product with desired properties which depends on final sintering temperature. Flow chart of sample preparation is given above (figure 3.1). Detail process of Calcination, Pelletization and Sintering are given below.

3.1.2 Calcination

Calcination is a thermal treatment process in presence of air applied to ores and other solid materials to bring about a thermal decomposition phase transition or removal of a volatile fraction. The calcination processes normally take place below the melting point of the product materials. Calcination is to be distinguished from roasting, in which more complex gas solid reaction take place between the furnace atmospheres of the solid. The calcination reaction usually takes place at or above the thermal decomposition or transition temperature. This temperature is usually defined as the temperature at which the standard Gibbs free energy for a particular calcination reaction is zero [1]. The calcining process can be repeated several times to obtain a high degree of homogeneity. The calcined powders are crushed into fine powders. The ideal characteristics of fine powders [2] are given below:

- 1) Small particle size (sub-micron)
- 2) Narrow distribution in particle size
- 3) Dispersed particles
- 4) Equiaxed shape of particles
- 5) High purity
- 6) Homogeneous composition.

A small particle size of the reactant powders provides a high contact surface area for initiation of the solid state reaction; diffusion paths are shorted, leading to more efficient completion of the reaction. Porosity is easily eliminated if the initial pores are very small. A narrow size distribution of spherical particles as well as a dispersed state is important for compaction of the

powder during green-body formation. Grain growth during sintering can be better controlled if the initial size is small and uniform.

3.1.3 Pelletization

It is a process of pressing the powder in uni-axial hydraulic press at room temperature by applying a force on to accelerate the reaction rate. Here we have to increase the area of contact between the particles, this can be achieved by pressing the reaction powder into pellets but even at high pressure the pellets are usually porous and the crystal contacts are not maximized. Typically cold pressed pellets are 20% to 40% porous. Depending upon requirement of our sample formation, sometimes hot press is required. So that the combined effect of temperature and pressing may cause the particle to fit together better but densification process is usually slow and may require several hours [3].

3.1.4 Sintering

Sintering is defined as the process of obtaining a dense, tough body by heating a compacted powder for a certain time at a temperature high enough to significantly promote diffusion, but clearly lower than the melting point of the main component. The driving force for sintering is the reduction in surface free energy of the powder. Part of this energy is transferred into interfacial energy (grain boundaries) in the resulting polycrystalline body [2, 4]. The sintering time, temperature and the furnace atmosphere play very important role on the dielectric, electric and magnetic properties of magnetic materials. The purposes of sintering process are:

- 1) To bind the particles together so as to impart sufficient strength to the product,
- 2) To densify the material by eliminating the pores, and
- 3) To homogenize the materials by completing the reactions left unfinished in the calcining step.

Sintering of crystalline solids is dealt by Coble and Burke [5] who found the following empirical relationship regarding rate of grain growth:

$$\bar{d} = kt^n \quad \dots \dots \dots (3.1)$$

Where, \bar{d} is the mean grain diameter, n is about 1/3, t is sintering time and k is a temperature dependent parameter. Sintering process is divided into several stages [2, 4], figure 3.2.

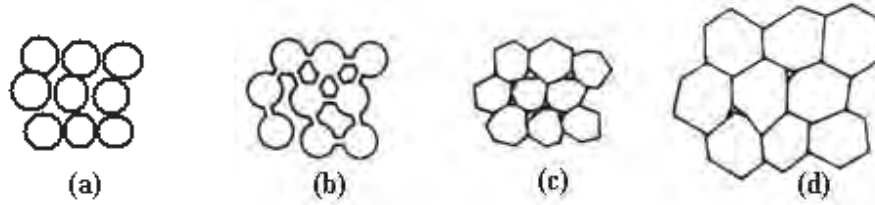


Figure 3.2: Schematic representation of sintering stages: (a) greenbody, (b) initial stage, (c) intermediate stage, and (d) final stage.

- Stage 1. Contact area between particles increases,
- Stage 2. Porosity changes from open to closed porosity,
- Stage 3. Pore volume decreases; grains grow.

In the initial stage, neighboring particles form a neck by surface diffusion and presumably also at high temperatures by an evaporation-condensation mechanism. Grain growth begins during the intermediate stage of sintering. Since grain boundaries are the sinks for vacancies, grain growth tends to decrease the pore elimination rate due to the increase in distance between pores and grain boundaries, and by decreasing the total grain boundary surface area. In the final stage, the grain growth is considerably enhanced and the remaining pores may become isolated.

3.2 Synthesis of Composition

The polycrystalline samples having compositions $\text{Bi}_{0.9}\text{Gd}_{0.1}\text{Fe}_{1-x}\text{Ti}_x\text{O}_3$ ($x = 0.00-0.25$) were synthesized by using standard solid state reaction technique. The high purity oxides of Bi_2O_3 , Gd_2O_3 , Fe_2O_3 , and TiO_2 powders were carefully weighed in stoichiometric proportion mixed thoroughly with acetone and grounded in an agate mortar until a homogeneous mixture was formed. The compacted mixtures of reagents taken in desired cation ratios were calcined at 800 °C for 1.5 h in a programmable furnace. The calcined powders were grounded again for 2 h to get more homogeneous mixture. The powders were pressed into pellets of thickness 1mm and diameter 12mm by using a uniaxial

hydraulic press and sintered at 825 °C for 5 h at heating rate 10 °C per minute. The crystal structure of the samples (sintered powder) was determined from x-ray diffraction (XRD) data. XRD patterns were collected at RT using a diffractometer (Rigaku Ultimate VII) with CuK α ($\lambda = 1.5418 \text{ \AA}$) radiation. The microstructure of the surface of pellets was observed using a field emission scanning electron microscope (FESEM, JEOL, JSM 5800) equipped with the energy dispersive x-ray (EDX). The EDX analysis has been used to determine the overall chemical homogeneity and composition of the samples. The dielectric properties were measured at RT using an impedance analyzer (Agilent 4294 A) in the frequency range of 100 Hz–20MHz. The magnetic properties of the samples were characterized by using a Vibrating Sample Magnetometer (VSM, Lakeshore 7407 series) with a sensitivity of 10^{-6} emu at RT.

3.3 Characterization Techniques

3.3.1 X-Ray Diffraction Analysis

X-Ray diffraction is one of the X-Ray scattering techniques, which are non destructive analytical technique revealing information about the crystallographic structure, chemical composition, and physical properties of materials. When X-rays interact with a crystalline substance (Phase), one gets a diffraction pattern. An electron in an alternating electromagnetic field will oscillate with the same frequency as the field. When an X-ray beam hits an atom, the electrons around the atom start to oscillate with the same frequency as the incoming beam. In almost all directions we will have destructive interference, that is, the combining waves are out of phase and there is no resultant energy leaving the solid sample. XRD is based on constructive interference of monochromatic X-Rays and a crystalline sample. The monochromatic X-rays are generated by a cathode ray tube, filtered to produce monochromatic radiation, collimated to concentrate them and directed toward the sample. The interaction of the incident rays with the sample produces constructive interferences (and a diffracted ray), when conditions satisfy Bragg's law. In accordance with Bragg's law when X-rays hit an atom, they make the electronic cloud move as does any electromagnetic wave. The interference is constructive when the phase shift is a multiple of 2π ; this condition can be expressed by Bragg's law: $n\lambda = 2d\sin\theta$. This law relates the wavelength of electromagnetic radiation

(λ) to the diffraction angle (Θ), and the lattice spacing (d) in a crystalline sample. these diffracted X-rays are then detected, processed and counted.

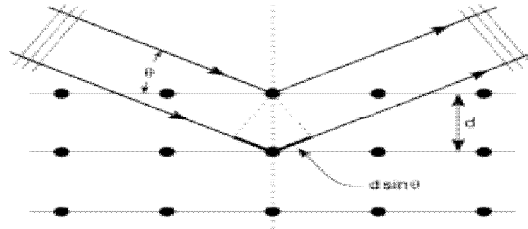


Figure 3.3: Bragg's law of diffraction.

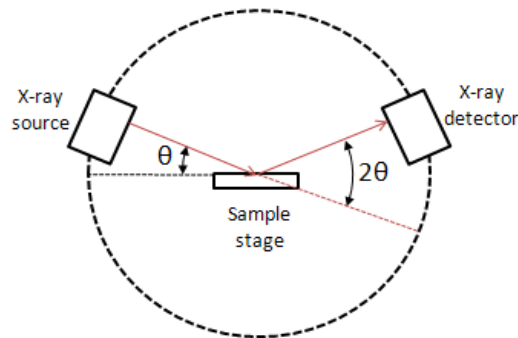


Figure 3.4: The schematic diagram shows the operation of XRD.

By scanning the sample through a range of angles, all possible diffraction directions of the lattice should be attained, due to the random orientation of the powdered material. conversion of the diffraction peaks to d -spacings allows identification of the mineral because each mineral has a set of unique d -spacings. Typically this is achieved by comparison of d -spacings with standard reference pattern. The orientation and interplanar spacing of these planes are defined by the three integers ($h k l$) called indices. A given set of planes with indices ($h k l$) cut the a -axis of the unit cell in h sections, the b -axis in k sections and the c -axis in l sections. A zero indicates that the planes are parallel to the corresponding axis, e.g. the ($2 2 0$) planes cut the a and the b axes in half, but are parallel to the c axis.



Figure 3.5: X-ray diffraction analysis machine.

3.3.2 Scanning Electron Microscope (SEM)

SEM is a type of electron microscope that creates various images (surface morphology) by focusing a high energy beam of electrons onto the surface of a sample and detecting signals from the interaction of the incident electron with the sample's surface. The type of signals gathered in a SEM varies and can include secondary electrons, characteristic x-rays, and back scattered electrons. In a SEM, these signals come not only from the primary beam impinging upon the sample, but from other interactions within the sample near the surface. The SEM is capable of producing high resolution images of a sample surface in its primary use mode, secondary electron imaging. Due to the manner in which this image is created, SEM images have great depth of field yielding a characteristic

three-dimensional appearance useful for understanding the surface structure of a sample. This great depth of field and the wide range of magnifications are the most familiar



Figure 3.6: Photograph of Scanning Electron Microscope (SEM).

imaging mode for specimens in the SEM. Characteristic x-rays are emitted when the primary beam causes the ejection of inner shell electrons from the sample and are used to tell the elemental composition of the sample. The back-scattered electrons emitted from the sample may be used alone to form an image or in conjunction with the characteristic x-rays as atomic number contrast clues to the elemental composition of the sample. The microstructure of the surface of the sintered pellets was observed using a field emission scanning electron microscope (FESEM, JEOL, JSM 5800).

3.3.2.1 Scanning Process and Image Formation

In a typical SEM, an electron beam is thermionically emitted from an electron gun fitted with a tungsten filament cathode. Tungsten is normally used in thermo ionic electron guns because it has the highest melting point and lowest vapor pressure of all metals, thereby allowing it to be heated for electron emission, and because of its low cost. The

electron beam, which typically has an energy ranging from a few 100 eV to 40 keV, is focused by one or two condenser lenses to a spot about 0.4 nm to 5 nm in diameter. The beam passes through pairs of scanning coils or pairs of deflector plates in the electron column, typically in the final lens, which deflect the beam in the x and y axes so that it scans in a raster fashion over a rectangular area of the sample surface.

When the primary electron beam interacts with the sample, the electrons lose energy by repeated random scattering and absorption within a teardrop-shaped volume of the specimen known as the interaction volume, which extends from less than 100 nm to around 5 μm into the surface. The size of the interaction volume depends on the electron's landing energy, the atomic number of the specimen and the specimen's density. The energy exchange between the electron beam and the sample results in the reflection of high-energy electrons by elastic scattering, emission of secondary electrons by inelastic scattering and the emission of electromagnetic radiation, each of which can be detected by specialized detectors. The beam current absorbed by the specimen can also be detected and used to create images of the distribution of specimen current. Electronic amplifiers of various types are used to amplify the signals which are displayed as variations in brightness on a cathode ray tube. The raster scanning of the CRT display is synchronized with that of the beam on the specimen in the microscope, and the resulting image is therefore a distribution map of the intensity of the signal being emitted from the scanned area of the specimen. The image may be captured by photography from a high resolution cathode ray tube, but in modern machines is digitally captured and displayed on a computer monitor.

3.3.2.2 Energy Dispersion X-Ray Spectroscopy

EDS or, EDX is an analytical technique which is used for the elemental analysis or chemical characterization of a sample. It is one of the variants of X-ray fluorescence spectroscopy relies on the analysis of a sample through interactions between electromagnetic radiation and matter, analyzing X-rays emitted by the matter in response to being hit with charged particles. Its characterization capabilities are due in large part to the fundamental principle that each element has a unique atomic structure allowing X-rays that are characteristic of an element's atomic structure to be identified uniquely from

one another. An EDX system is comprised of four components: the excitation source (electron beam or x-ray beam), the X-ray detector, the pulse processor, the analyzer.

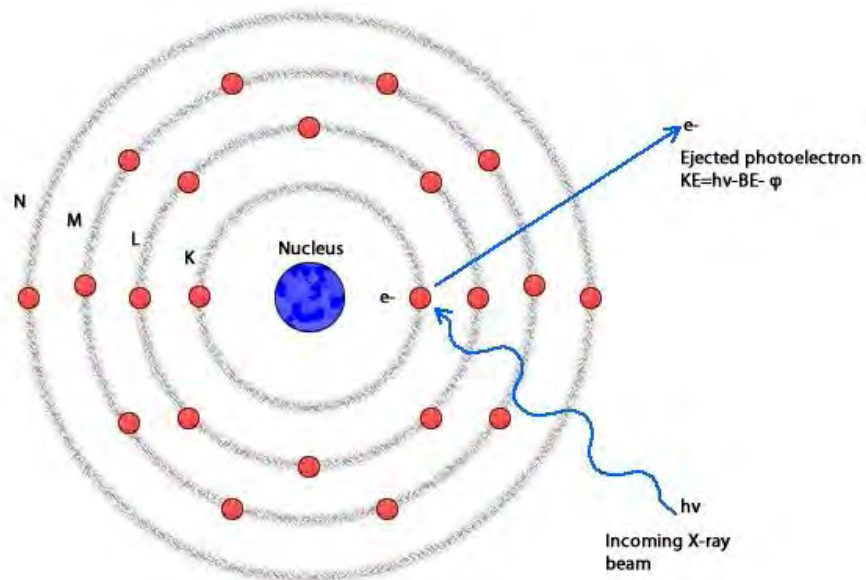


Figure 3.7: Principle of EDX.

The incident beam may excite an electron in an inner shell, ejecting it from the shell while creating an electron hole. An electron from an outer, higher-energy shell then fills the hole, and the difference in energy between the higher-energy shell and the lower energy shell may be released in the form of an X-ray. The number and energy of the X-rays emitted from a specimen can be measured by an energy dispersive spectrometer. As the energy of the X-rays are characteristic of the difference in energy between the two shells, and of the atomic structure of the element from which they were emitted, this allows the elemental composition of the specimen to be measured.

3.3.3 X-Ray Photoelectron Spectroscopy (XPS)

XPS works on the principle of photoelectric effect discovered by Heinrich Hertz in 1887. Upon radiation of appropriate energy incident, electrons are emitted from the surface of the metal. The relation between the energy of the excitation radiation, work function of the metal and the maximum kinetic energy of the emitted electron as proposed by Einstein in 1905 is:

$$h\nu = \phi + KE_{\max} \dots\dots\dots(3.2)$$

‘ Φ ’ is the work function of the metal, ‘ $h\nu$ ’ is the energy of the radiation, ‘ KE_{\max} ’ is the maximum kinetic energy of the emitted electron. For analysing the core electronic structure (0 – 1300 eV) of elements, radiation of high energy were used like X-rays, hence the corresponding spectroscopy is termed X-ray Photoelectron Spectroscopy (XPS) (Figure 3.8). Surface analysis by XPS is accomplished by irradiating a sample with monoenergetic soft X-rays and analysing the energy of the detected electrons. Mg $K\alpha$ (1253.6 eV), Al $K\alpha$ (1486.6 eV), or monochromatic Al $K\alpha$ (1486.7 eV) X-rays are usually used. These photons have limited penetrating power in a solid of the order of 1 – 10 μm . They interact with atoms in the surface region, causing electrons to be emitted by the photoelectric effect. The emitted electrons have measured kinetic energies given by:

$$KE = h\nu - BE - \phi_s \dots\dots\dots(3.3)$$

where ‘ $h\nu$ ’ is the energy of the photon, ‘ BE ’ is the binding energy of the atomic orbital from which electron originates, ‘ Φ_s ’ is the work function of the spectrometer. The binding energy may be regarded as the energy difference between the initial and final states after the photoelectron has left the atom.

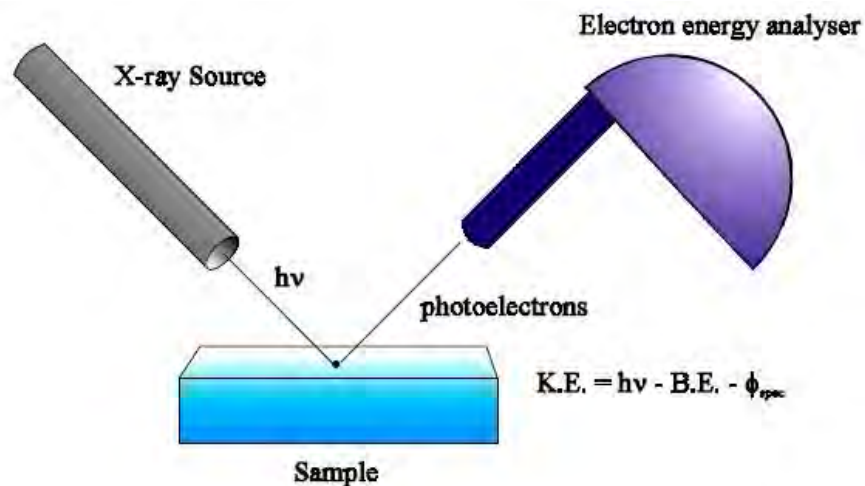


Figure 3.8: Schematic diagram of a typical X-ray photoelectron spectroscopy (XPS).

Because, there are a variety of possible final states of the ions from each type of atom, there is a corresponding variety of kinetic energies of the 50 emitted electrons. Moreover

there is a different probability or cross section for each final state. Because each element has unique set of binding energies, XPS can be used to identify and determine the concentration of the elements in the surface. Variation in the elemental binding energies (the chemical shifts) arise from differences in the chemical potential and polarizability of compounds. These chemical shifts can be used to identify the chemical state of the material being analysed. In our studies, X-ray photoelectron spectroscopy (XPS, ULVAC-PHI Inc., Model 1600) analysis was carried out with a Mg- K_{α} radiation source.

3.3.4 Dielectric Properties Measurement

The dielectric properties were measured at room temperature using an impedance analyzer (Agilent 4294 A) in the frequency range of 100 Hz–20MHz. A dielectric is an electrical insulator that may be polarized by the action of an applied electric field. When a dielectric material is placed in an electric field, electric charge do not flow through the material, as in a conductor, but only slightly shift from their average equilibrium positions causing dielectric polarization: positive charges are displaced along the field and negative charges shift in the opposite direction. Dielectric typically means materials with a high polarizability. The latter is expressed by a number called the relative permittivity (also known in older texts as dielectric constant). A common example of a dielectric is the electrically insulating material between the metallic plates of a capacitor. The polarization of the dielectric by the applied electric field increases the capacitor's surface charge for the given electric field strength. The dielectric properties were measured using Wayne Kerr impedance analyzer 6500 B series. Measurements of dielectric properties normally involve the measurements of the change in capacitance and loss of a capacitor in presence of the dielectric materials. The behavior of a capacitance can now be described as follows. Here an ideal loss less air capacitor of capacitance C_0 . On insertion of a dielectric material in a space the capacitance will be changed. The dielectric constant (ϵ) and electrical properties measurements on disk-spaced specimens will be carried out at roomtemperature on all the samples in the high frequency range. The dielectric constant ϵ will be calculated using the following relations, $\epsilon = C/C_0$ and $\epsilon = \epsilon_0 \epsilon_r$. where, C is thecapaciatance of the sample and $C_0 = \epsilon_0 A/d$, is derived geometrically.

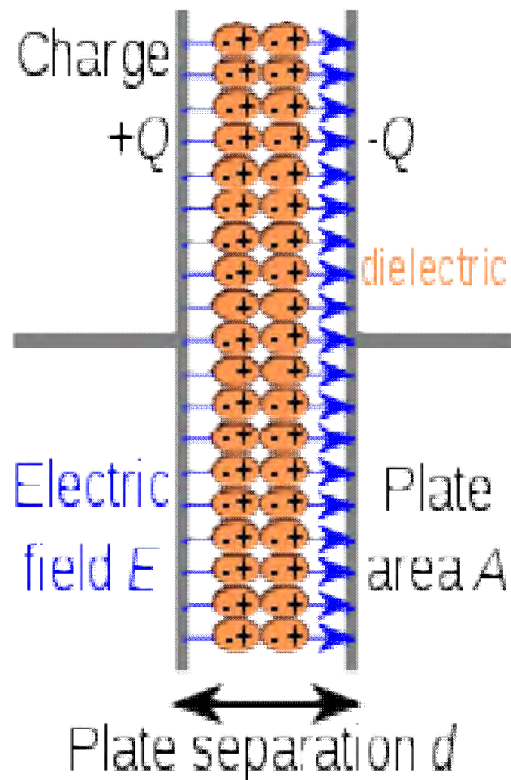


Figure 3.9: Diagram of dielectric plate.

Here, C_0 is the capacitance of the capacitor without the dielectric materials, d is the thickness of the capacitor and $A(= \pi r^2)$ is the area of cross section of the disk space sample. For the measurement of dielectric properties the samples will be painted on either side with silver paste to ensure good electric contacts.

3.3.5 Magnetic Properties Measurement

The vibrating sample magnetometer (VSM) is a fast and sensitive DC magnetometer. The basic measurement is accomplished by oscillating the sample near a detection coil and synchronously detecting the voltage induced. By using a compact gradiometer pick-up coil configuration, a relatively large oscillation amplitude (1-3 mm peak), and a frequency of 40 Hz, the system can resolve magnetization changes of less than 10^{-6} emu at a data range of 1 Hz by vibrating the sample sinusoidally, the induced voltage due to

the magnetic moment in the pick up coil is proportional to the samples magnetization but does not depend on the strength of the applied magnetic field.



Figure 3.10: The Lakeshore vibrating sample magnetometer (VSM).

Therefore, by detecting the induced magnetic voltage, it is possible to measure the magnetic field dependent magnetization hysteresis curve of the materials.

Reference:

- [1] Goldman A., "Handbook of Modern Ferromagnetic Materials", Kulwer Acad. Pub, Boston, U.S.A, 1999.
- [2] Valenzuela R., "Magnetic Ceramics", Cambridge University Press, Cambridge, 1994.
- [3] West, A. R., "Solid state chemistry and its applications", John Willey Sons, 1987.
- [4] Kingery W. D., Bowen H. K. and Uhlman D. R., "Introduction to Ceramics", 2nd edition, Wiley Interscience, New York, 476, 1976.
- [5] Coble R. L. and Burke J. E., "On the Reactivity of Solids", 4th Int. Symp. Amsterdam, 38-51, 1960.
- [6] McColm I. J. and Clark N. J., "Forming, Shaping and Working of high Performance Ceramics", Blackie, Glasgow, 1-338, 1988.

Chapter 4

Results and Discussion

The nominal compositions of $\text{Bi}_{0.9}\text{Gd}_{0.1}\text{Fe}_{1-x}\text{Ti}_x\text{O}_3$ ($x = 0.00 - 0.25$) ceramics were synthesized by conventional solid state reaction technique and their structure, morphology, dielectric, and magnetic properties were investigated and discussed. Investigation of the surface morphology and the structure of the samples were done by using scanning electron microscopy (SEM) and X-ray diffraction techniques, respectively. The concentration of oxygen vacancies in each composition was detected by the help X-ray photoelectron spectroscopy (XPS) technique. The dielectric properties of this multiferroics were determined as a function of frequencies, and the measurements of magnetic properties were obtained using Vibrating Sample Magnetometer (VSM). The outcomes of this investigation were presented in this chapter.

4.1 Structural Characterizations

4.1.1 X-Ray Diffraction

The XRD patterns of the $\text{Bi}_{0.9}\text{Gd}_{0.1}\text{Fe}_{1-x}\text{Ti}_x\text{O}_3$ ($x = 0.00 - 0.25$) ceramics sintered at temperature of their optimum density as shown in figure 4.1 (a), indicate the formation of polycrystalline structure. There are small traces of secondary phase $\text{Bi}_2\text{Fe}_4\text{O}_9$ as labeled by ∇ still appear both in the undoped and doped samples. The apparently unavoidable formation of secondary phases during the solid-state synthesis of BiFeO_3 based materials have been reported in several articles [1,2,3]. However, the presences of secondary phases do not affect ferroelectric and magnetic properties of the samples because these phases are neither magnetic nor ferroelectric at RT [2]. The decrease in the peak intensities for $x = 0.05 - 0.25$ indicates the incorporation of Ti in $\text{Bi}_{0.9}\text{Gd}_{0.1}\text{Fe}_{1-x}\text{Ti}_x\text{O}_3$ ceramics [2,4,5]. Furthermore, the twin peaks observed around $2\theta \approx 40^\circ$, 52° , and 57° merges to form a broadened peak [2,4] also confirms the substitution of Ti in these compounds. Splitting of peak around $2\theta \approx 32^\circ$ as Ti content increases to $x = 0.25$ suggests a structure change from rhombohedral to orthorhombic [6] and is consistent with that of reported articles [7,8]. It would be excellent to perform Rietveld refinement of XRD patterns to obtain any lattice distortion occurred during substitution/co-substitution and

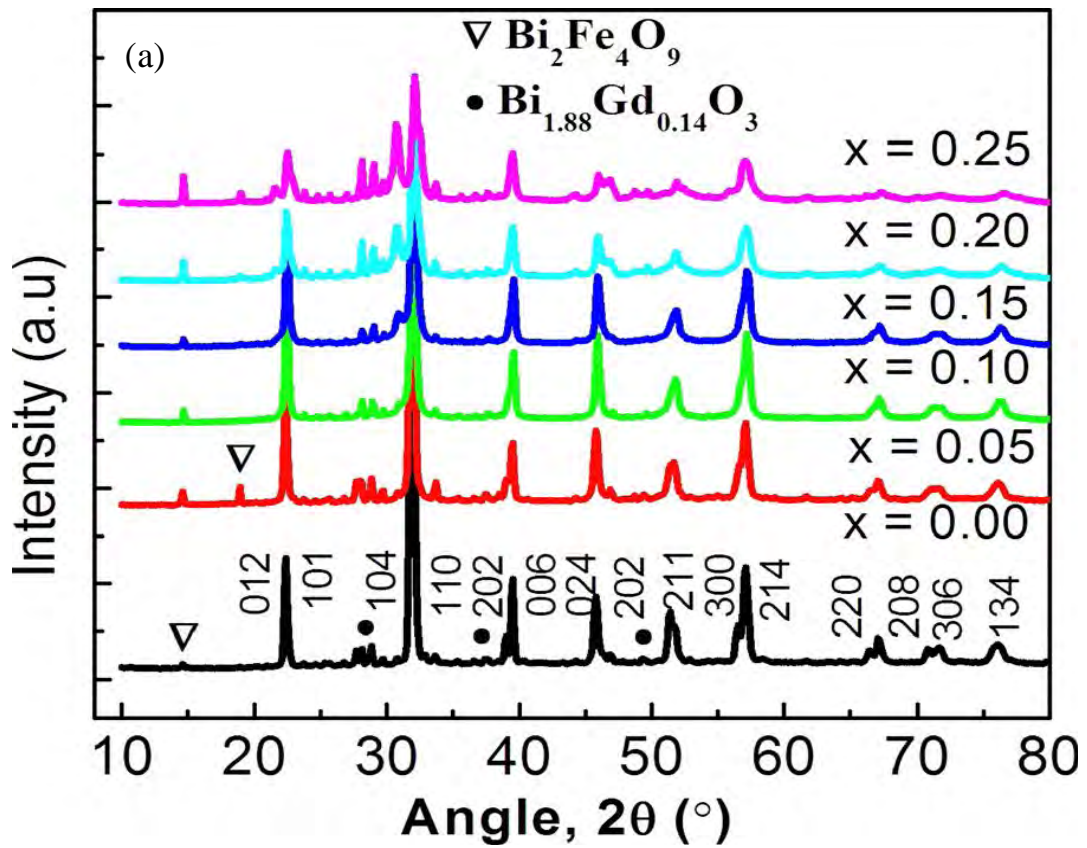


Figure 4.1: (a) X-ray diffraction patterns of $\text{Bi}_{0.9}\text{Gd}_{0.1}\text{Fe}_{1-x}\text{Ti}_x\text{O}_3$ ($x = 0.00 - 0.25$) ceramics.

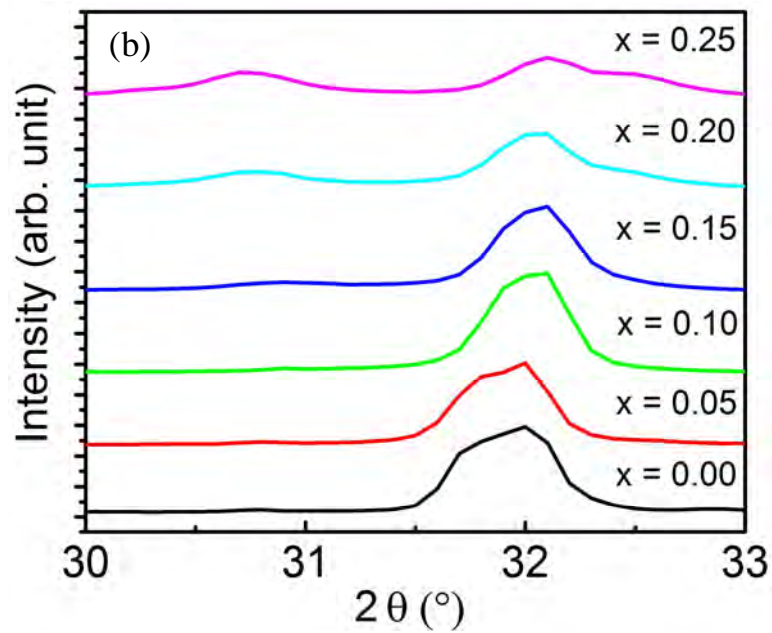


Figure 4.1: (b) Splitting of peak around $2\theta \approx 32^\circ$ as Ti content increases to $x = 0.25$.

unit cell parameters could be measured accurately, however, at the moment we are not capable to perform Rietveld refinement.

4.1.2 Morphological Studies

To investigate the microstructure of the surface of the pellets, FESEM imaging was carried out for all of the samples. Figure 4.2(a) demonstrates the surface morphology of the pellet of the 10% Gd doped $\text{Bi}_{0.9}\text{Gd}_{0.1}\text{FeO}_3$ sample (hereafter referred as Ti undoped $\text{Bi}_{0.9}\text{Gd}_{0.1}\text{FeO}_3$ sample). Notably, in the nominal compositions of $\text{Bi}_{0.9}\text{Gd}_{0.1}\text{Fe}_{1-x}\text{Ti}_x\text{O}_3$ ceramics, it is expected that titanium is in its tetravalent state and the non magnetic Ti^{4+} substitutes Fe^{3+} . This is in fact not very simple because in order to accommodate a charge balance some Fe must be present as Fe^{2+} or there must be present some type of non-stoichiometry. Figure 4.2(b) shows the microstructure of the Ti doped $\text{Bi}_{0.9}\text{Gd}_{0.1}\text{Fe}_{0.9}\text{Ti}_{0.1}\text{O}_3$ ceramic with $x = 0.10$ as a representative of the $x = 0.15$ and 0.20 ceramics. Figure 4.2(c) is an FESEM image of 25% Ti doped (the highest doping concentration) sample $\text{Bi}_{0.9}\text{Gd}_{0.1}\text{Fe}_{0.75}\text{Ti}_{0.25}\text{O}_3$ which also represents $x = 0.05$ ceramic. Insets of figures 4.2(a) and 4.2(b) show the histograms of the grain size distributions of the respective micrographs. It is clear from figures 4.2(a) and 4.2(b) and their respective histograms that the average grain size is reduced from $\sim 1.5 \mu\text{m}$ to $\sim 200 \text{ nm}$ with increasing Ti concentration. Previous studies demonstrated that undoped BiFeO_3 had a dense microstructure with an average size of ~ 5 to $\sim 15 \mu\text{m}$ [9,10]. In our investigation, we have also observed that the average grain size of pure BiFeO_3 is around $\sim 5 \mu\text{m}$ (data not shown here). Therefore, unlike the non-modified BiFeO_3 sample, the average grain size of the Ti undoped, i.e., 10% Gd doped $\text{Bi}_{0.9}\text{Gd}_{0.1}\text{FeO}_3$ sample is $\sim 1.5 \mu\text{m}$ which is well consistent with previous investigation [6]. For the samples with $x = 0.05$, that is for an increase of 5% Ti in $\text{Bi}_{0.9}\text{Gd}_{0.1}\text{Fe}_{1-x}\text{Ti}_x\text{O}_3$, a decreasing trend of the average grain size to $\sim 200 \text{ nm}$ was observed, however, the grain distribution was not quite homogeneous rather there were couple of grains with larger sizes ($\sim 1 \mu\text{m}$) in this sample as was shown in figure 4.2(c). The further increase of the Ti content to 10% ($x = 0.10$) reduced the average grain size to $\sim 200 \text{ nm}$ as well as made the distribution of the grains homogeneous (Figure 4.2(b)). Notably, increase of the Ti content from $x = 0.10$ to $x = 0.15$ or 0.20 does not reduce anymore the average grain size from $\sim 200 \text{ nm}$. Due to the

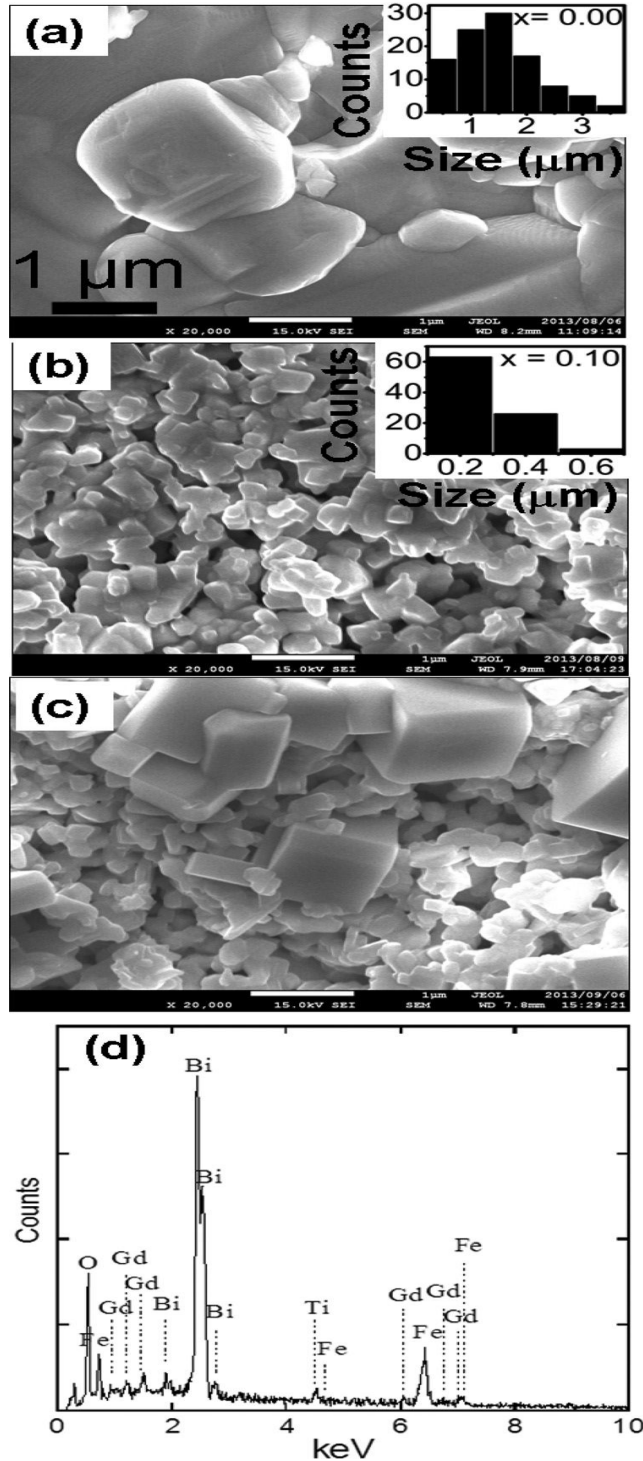


Figure 4.2: FESEM micrograph of Bi_{0.9}Gd_{0.1}Fe_{1-x}Ti_xO₃ ceramics: (a) x = 0.00, (b) x = 0.10 and (c) x = 0.25. Inset: respective histograms of images (a) and (b). (d) Shows an EDX pattern recorded from image (b).

substitution of Ti, the average grain size was reduced and the peak in the XRD pattern of the Ti substituted sample was widened as shown in figure 4.1.

However, for 25% Ti doping, the average grain size remain unchanged, that is 200 nm but some of the grains grow to larger sizes ($\sim 1 \mu\text{m}$) (Figure 4.2(c)). Previous investigation suggested that the grain growth depends upon the concentration of oxygen vacancies [11] and diffusion rate of the ions. Large number of oxygen vacancies are generate in pure BiFeO_3 due to highly volatile nature of Bi. An increment of the Ti doping concentration in $\text{Bi}_{0.9}\text{Gd}_{0.1}\text{Fe}_{1-x}\text{Ti}_x\text{O}_3$ decreased the average grain size significantly due to the fact that Ti possesses a higher valence than Fe and suppresses the formation of oxygen vacancies. Therefore, the significant reduction of the average grain size in Gd and Ti co-doped BiFeO_3 samples could be interpreted by the suppression of the formation of oxygen vacancies because of the requirements of the charge compensation. The decreased oxygen vacancies lead to a lower grain growth rate which is actually a consequence of slower oxygen ion motion [12]. To ascertain the level of doping in these samples, EDX analysis was done on all of them. Figure 4.2(d) is an EDX spectrum of the $\text{Bi}_{0.9}\text{Gd}_{0.1}\text{Fe}_{0.9}\text{Ti}_{0.1}\text{O}_3$ sample taken from image 4.2(b) as a representative of all other samples. This EDX spectrum of the $\text{Bi}_{0.9}\text{Gd}_{0.1}\text{Fe}_{0.9}\text{Ti}_{0.1}\text{O}_3$ ceramic shown in figure 4.2(d) confirms the presence of expected amounts of Bi, Gd, Fe, Ti, and O in the synthesized sample.

4.1.3. XPS Analysis

To identify the chemical binding of Gd and Ti co-doped BiFeO_3 ceramics as well as to know the concentration of oxygen related defects we have carried out XPS analysis. The XPS spectra of $\text{Bi}_{0.9}\text{Gd}_{0.1}\text{Fe}_{0.9}\text{Ti}_{0.1}\text{O}_3$ ceramic as a typical example is shown in figure 4.3 (a). The binding energy values of Bi, Gd, Fe, Ti and O confirmed the phase purity of the compound. It is reported that the absence of oxygen vacancies in multiferroic materials might reduce the leakage currents [13] and improve magnetoelectric properties. Therefore, we tried to estimate qualitatively the concentration of oxygen vacancies from XPS measurements.

As presented in figure 4.3 (b), the O 1s XPS spectra of bulk BiFeO_3 and $\text{Bi}_{0.9}\text{Gd}_{0.1}\text{Fe}_{1-x}\text{Ti}_x\text{O}_3$ ($x = 0.00 - 0.25$) ceramics demonstrate an asymmetric peak at 529.8 eV along with an additional peak. The asymmetric curves of the bulk samples can be Gaussian

fitted by two symmetrical as shown in figure 4.3 (b). The lower binding energy peak is corresponds the O 1s core spectrum, while higher binding energy peak is attributed to the oxygen vacancies i.e. to the oxygen related defects [14] in the sample. It is evident from figure 4.3 (b) that the higher binding energy peak is related to oxygen vacancy is much more prominent in undoped BiFeO₃ ceramic compared than that of other compounds. Upon the substitution of Gd as well as co-substitution of Gd and Ti in BiFeO₃ reduce the oxygen vacancies compared than that of BiFeO₃. The complete reduction of oxygen vacancies is possible only if phase pure nanoparticles of this ceramic system can be prepared and this will be discussed again in chapter 5.

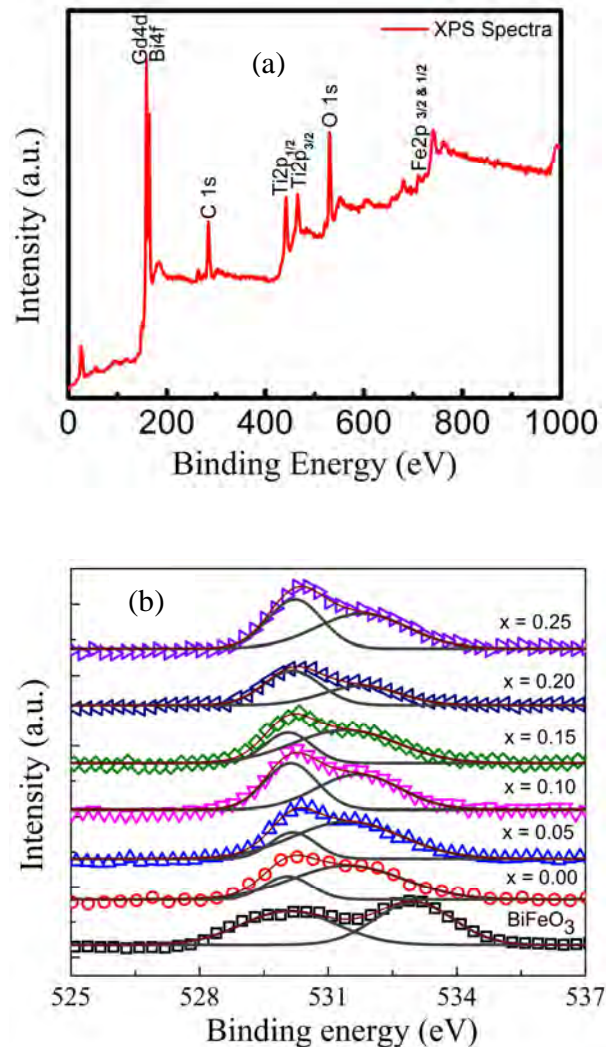


Figure 4.3: (a) XPS spectra of Bi_{0.9}Gd_{0.1}Fe_{0.9}Ti_{0.1}O₃ ceramic system as a representative of other compositions. (b) The O 1s core spectrum and oxygen vacancy peaks for all compositions.

4.2 Dielectric Measurements

Figure 4.4(a) illustrates the frequency dependence of the dielectric constant (ϵ') of $\text{Bi}_{0.9}\text{Gd}_{0.1}\text{Fe}_{1-x}\text{Ti}_x\text{O}_3$ ceramics with (a) $x = 0.00$, (b) $x = 0.05$, (c) $x = 0.10$, (d) $x = 0.15$, (e) $x = 0.20$ and (f) $x = 0.25$ measured at RT in the frequency range 100 Hz – 20MHz. The variation of dielectric loss tangent ($\tan\delta$) in the same frequency range is shown in figure 4.4(b).

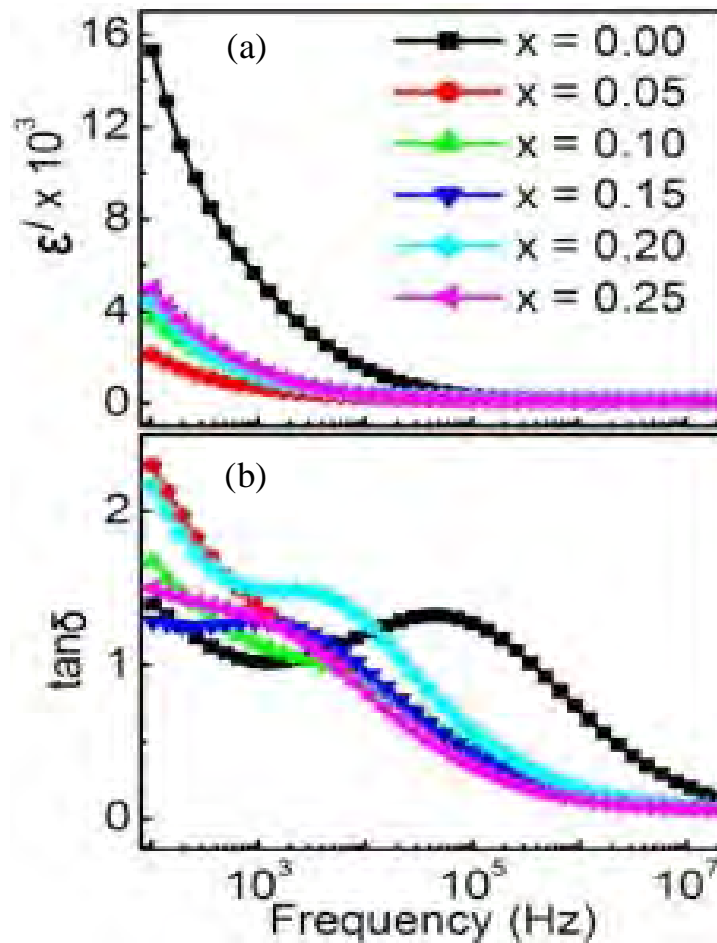


Figure 4.4: (a) Semi-log plot of dielectric constant of $\text{Bi}_{0.9}\text{Gd}_{0.1}\text{Fe}_{1-x}\text{Ti}_x\text{O}_3$ ceramics: (a) $x = 0.00$ (b) $x = 0.05$ (c) $x = 0.10$ (d) $x = 0.15$ (e) $x = 0.20$ and (f) $x = 0.25$ recorded at RT in the wide frequency range from 100 Hz to 20 MHz. (b) Variation in $\tan\delta$ as a function of frequency at RT.

The dielectric constant of Ti undoped sample $\text{Bi}_{0.9}\text{Gd}_{0.1}\text{FeO}_3$ ($x = 0.00$) is maximum at the lower frequencies which decreases sharply with increasing frequency up to about

300 kHz and then becomes almost constant at higher frequencies >300 kHz. Gd and Ti co-doped $\text{Bi}_{0.9}\text{Gd}_{0.1}\text{Fe}_{1-x}\text{Ti}_x\text{O}_3$ ($x = 0.05 - 0.25$) ceramics also demonstrate slight dispersion at low frequency and a frequency independent behavior in a wide range of high frequencies. This low frequency dispersion is common in dielectric and ferroelectric materials [15] and explained in the light of space charge polarization as discussed by Maxwell [16] and Wagner [17]. At low frequencies, the space charges are able to follow the frequency of the applied field, while at a high frequency they may not have time to build up and undergo relaxation. The observed large values of dielectric constant at low frequencies for $\text{Bi}_{0.9}\text{Gd}_{0.1}\text{Fe}_{1-x}\text{Ti}_x\text{O}_3$ ceramics ($x = 0.00 - 0.25$) attributed to the interfacial polarization due to high concentration of oxygen vacancies. The oxygen vacancies are produced due to highly volatile nature of Bi, and /or multiple oxidation states of Fe (Refs. 18 and 19) as was also mentioned earlier. The value of the frequency dependent dielectric constant may be described in two-step. First, the dielectric constant is decreased due to Ti substitution compared to that of Ti undoped sample.

For the smallest amount of Ti dopant (05%) introduced in $\text{Bi}_{0.9}\text{Gd}_{0.1}\text{Fe}_{1-x}\text{Ti}_x\text{O}_3$, the dielectric constant at 100 kHz drops to almost one eighth of its original value for Ti undoped $\text{Bi}_{0.9}\text{Gd}_{0.1}\text{FeO}_3$ sample. The dielectric constant at low frequencies is much smaller for all Gd and Ti co-doped samples $\text{Bi}_{0.9}\text{Gd}_{0.1}\text{Fe}_{1-x}\text{Ti}_x\text{O}_3$ ($x = 0.05 - 0.25$) compared to that of Ti undoped sample $\text{Bi}_{0.9}\text{Gd}_{0.1}\text{FeO}_3$.

Second, an increment of Ti doping concentration from 05% to 10, 15 and 20% increases the dielectric constant and then decreases again for 25% doping concentration. The dielectric constants of $\text{Bi}_{0.9}\text{Gd}_{0.1}\text{Fe}_{1-x}\text{Ti}_x\text{O}_3$ ($x = 0.00 - 0.25$) ceramics at high frequencies (50 kHz - 20 MHz) are inserted in table I. From the table, it is clear that in a wide range of high frequencies (50 kHz to 20 MHz), the dielectric constant of Gd and Ti co-doped samples with $x = 0.10, 0.15$ and 0.20 is higher than that of co-doped samples with $x = 0.05$ and 0.25 (marked by red). It is also noteworthy that the dielectric constant of Gd and Ti co-doped ceramics with $x = 0.10, 0.15$ and 0.20 is higher at any frequency than that of pure BiFeO_3 ceramics for which dielectric constant is around 100 as reported in reference 18. The higher values of the dielectric constants at high frequencies for samples with $x = 0.10, 0.15$ and 0.20 could be attributed to the reduced grain size of these compounds.

Table 4.1: Dielectric constant at different frequencies for $x = 0.00 - 0.25$. The table shows that in a wide range of high frequencies (50 kHz to 20000 kHz) the dielectric constant amongst co-doped ceramics is higher for $x = 0.10, 0.15$ and 0.20 compared to that of $x = 0.05$ and 0.25 samples.

Frequency (kHz)	Dielectric constant for $x =$					
	0.00	0.05	0.10	0.15	0.20	0.25
50	552	139	244	244	285	211
100	367	120	209	210	253	178
1000	142	91	154	158	205	128
10000	99	82	136	139	187	113
20000	96	81	134	137	184	112

The reduced grain size ultimately increased volume fraction of the grain boundaries leading to high dielectric constant. The dielectric constant was comparatively lower for samples with $x = 0.05$ and 0.25 although the average grain size was also smaller than that of Ti undoped sample. This might be due to the fact that the grain size distribution was not homogeneous for these two samples and there was grain growth of some of the grains to $\sim 1 \mu\text{m}$ (Figure 4.2(c)).

The frequency dependent region of dielectric constant decreased due to Ti substitution compared to that of Ti undoped sample. Due to 05% Ti doping, the frequency dependent region of the dielectric constant of sample $\text{Bi}_{0.9}\text{Gd}_{0.1}\text{Fe}_{0.95}\text{Ti}_{0.05}\text{O}_3$ is reduced to 30 kHz from 300 kHz of Ti undoped sample $\text{Bi}_{0.9}\text{Gd}_{0.1}\text{FeO}_3$. The frequency dependent region of all other Gd and Ti co-doped samples are also decreased compared to that of Ti undoped sample. This indicates that the extrinsic behavior (low frequency behavior) of these co-doped ceramics is suppressed with Ti doping concentration. It was already mentioned that Ti possesses a higher valence than Fe and the substitution of Ti suppresses the formation of oxygen vacancies because of the requirements of the charge compensation. The phenomenon of oxygen vacancies has direct correspondence with the leakage current density [9].

It is expected that leakage current densities in the Gd and Ti co-doped samples were decreased due to the low concentration of charge defects such as oxygen vacancies [9,19] as was observed from XPS measurements, and therefore, the low frequency dispersion was suppressed due to Ti substitution.

The dielectric loss tangent also shows frequency dependency as illustrated in figure 4.4(b). At low frequency, the dielectric loss is lower for Ti undoped sample $\text{Bi}_{0.9}\text{Gd}_{0.1}\text{FeO}_3$ compared to that of Gd and Ti co-doped samples. Interestingly, at high frequency, the loss tangent is higher for Ti undoped sample $\text{Bi}_{0.9}\text{Gd}_{0.1}\text{FeO}_3$ and lowers for all Gd and Ti co-doped samples. Due to the low (<0.15) loss tangent values at higher frequencies, the Gd and Ti co-doped samples might have potential applications in high-frequency microwave devices.

4.3 Magnetic Characterization

Magnetization experiments were carried out at RT using VSM. Figure 4.5(a) shows M-H curves for pure BiFeO_3 , Ti undoped $\text{Bi}_{0.9}\text{Gd}_{0.1}\text{FeO}_3$, and Gd and Ti co-doped $\text{Bi}_{0.9}\text{Gd}_{0.1}\text{Fe}_{1-x}\text{Ti}_x\text{O}_3$ ($x = 0.05 - 0.25$) ceramics measured at RT with an applied magnetic field of up to ± 12 kOe. All the samples show unsaturated magnetization loops which confirm the basic antiferromagnetic nature of the compounds. As is seen from figure 4.5(b) that pure BiFeO_3 sample possess a very narrow hysteresis loop with a very small but non-zero remanent magnetization (0.0009 emu/g) and a coercive field of ~ 110 Oe at RT. This is due to the fact that pure BiFeO_3 is antiferromagnetic (AFM) which does not possess any spontaneous magnetization [20] but has a residual magnetic moment for a canted spin structure.

Figures 4.5(c) – 4.5(h) demonstrate an enlarged view of the low-field M-H hysteresis loops of $\text{Bi}_{0.9}\text{Gd}_{0.1}\text{Fe}_{1-x}\text{Ti}_x\text{O}_3$ ceramics measured at RT with (c) $x = 0.00$ (d) $x = 0.05$ (e) $x = 0.10$ (f) $x = 0.15$, (g) $x = 0.20$ and (h) $x = 0.25$. From figures 4.5(c) – 4.5(h), a non-zero remanent magnetization and coercive field are observed. The remanent magnetization (M_r) is defined as $M_r = |(M_{r1} - M_{r2})| / 2$, where M_{r1} and M_{r2} are the magnetization with positive and negative points of intersection with $H = 0$, respectively [21], as shown in figure 4.5(h). The coercive field (H_c) is given by $H_c = |(H_{c1} - H_{c2})| / 2$, where H_{c1} and H_{c2} are the left and right coercive fields [22,23], respectively, as shown also in figure 4.5(h).

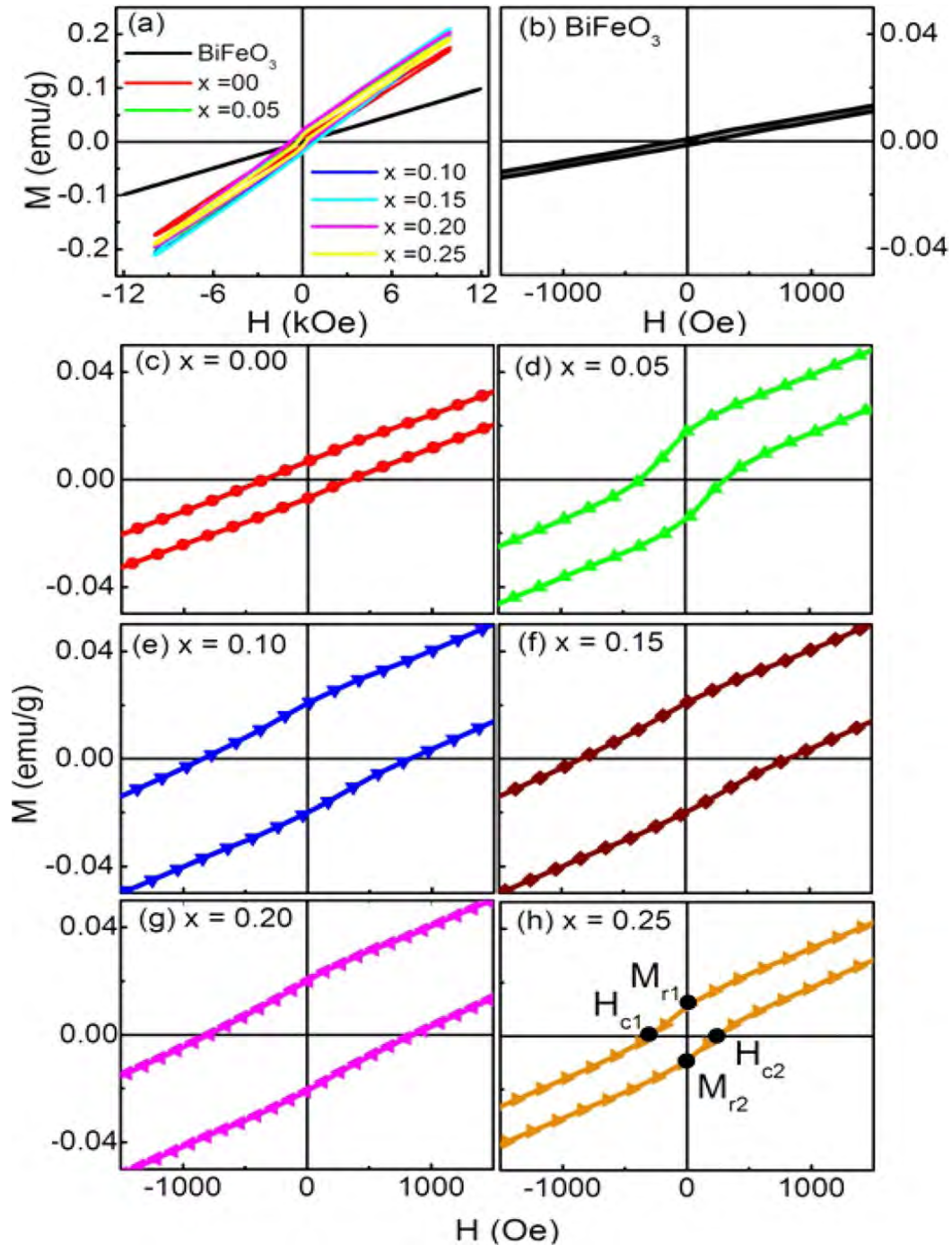


Figure 4.5: (a) M-H hysteresis loops of pure BiFeO₃ and Bi_{0.9}Gd_{0.1}Fe_{1-x}Ti_xO₃ (x = 0.00 – 0.25) ceramics at room temperature. (b) An enlarged view of the low-field M-H hysteresis loop of pure BiFeO₃. (c) – (h) An enlarged view of the low-field M-H hysteresis loops of Bi_{0.9}Gd_{0.1}Fe_{1-x}Ti_xO₃ samples obtained at RT: (c) x = 0.00 (d) x = 0.05 (e) x = 0.10 (f) x = 0.15 (g) x = 0.20 and (h) x = 0.25. (h) Also shows the left and right side coercive fields (H_{c1} and H_{c2}) and remanent magnetizations (M_{r1} and M_{r2}) of M-H loops. An asymmetric shifts both in the field and magnetization axes of Gd and Ti co-doped samples (d)-(h) indicates the existence of the EB phenomenon.

Calculated values of M_r and H_c were plotted in Figures 4.6(a) and 4.6(b), respectively, for $\text{Bi}_{0.9}\text{Gd}_{0.1}\text{Fe}_{1-x}\text{Ti}_x\text{O}_3$ ($x = 0.00 - 0.025$) ceramics. An increment of the 05% Ti doping concentration in place of Fe in $\text{Bi}_{0.9}\text{Gd}_{0.1}\text{Fe}_{1-x}\text{Ti}_x\text{O}_3$ increased the remanent magnetization at RT, although the coercivity remained unchanged as shown in figures 4.6(a) and 4.6(b). A further increase in Ti doping concentration to 10% dramatically enhanced M_r and H_c (Figures 4.6(a) and 4.6(b)). For any further increment of the Ti doping concentration from 10% to 15 and 20%, the remanent magnetizations and coercive fields were unaltered (Figures 4.6(a) and 4.6(b)) and highest. Due to 10% Gd doping in BiFeO_3 improved magnetic property was observed (Figure 4.5(c)) as was reported earlier in reference 24. This enhancement of the magnetization at RT was attributed [24] to the structural distortion in the perovskite with change in Fe – O – Fe angle. It was expected that this structural distortion could lead to suppression of the spin spiral and hence enhanced the magnetization in the $\text{Bi}_{0.9}\text{Gd}_{0.1}\text{FeO}_3$ system.

As in the case of 10% Gd doped $\text{Bi}_{0.9}\text{Gd}_{0.1}\text{FeO}_3$, the hysteresis loops of Gd and Ti co-doped ceramics were not really saturated at 12 kOe, however, a significant enhancement in remanent magnetization and coercive field was observed with the increase in Ti doping concentration in the $\text{Bi}_{0.9}\text{Gd}_{0.1}\text{Fe}_{1-x}\text{Ti}_x\text{O}_3$ system. In a similar investigation, room temperature magnetic properties were carried out for only Ti doped $\text{BiFe}_{1-x}\text{Ti}_x\text{O}_3$ ceramics with varying x up to 0.35 [6]. In that investigation, the highest remanent magnetization was 0.0095 emu/g (Ref. 6) for 20% Ti doped (not co-doped) sample $\text{BiFe}_{0.80}\text{Ti}_{0.20}\text{O}_3$. In the case of presently investigated Gd and Ti co-doped ceramics $\text{Bi}_{0.9}\text{Gd}_{0.1}\text{Fe}_{1-x}\text{Ti}_x\text{O}_3$ with $x = 0.10, 0.15, 0.20$, the remanent magnetization is 0.02 emu/g, which is double than that of only Ti doped $\text{BiFe}_{0.80}\text{Ti}_{0.20}\text{O}_3$ ceramic. However, there is a possibility that the observed magnetic behavior could be due to the presence of magnetic secondary phases which would not be detected by XRD technique because of its limit of detection. In another investigation, an improved magnetic behavior in Gd and Ti co-doped BiFeO_3 samples were observed [25] which was attributed to further suppression of spiral spin structure due to coexistence of rhombohedral and orthorhombic phases.

The coercive field is also higher for Gd and Ti co-doped samples $\text{Bi}_{0.9}\text{Gd}_{0.1}\text{Fe}_{1-x}\text{Ti}_x\text{O}_3$ with $x = 0.10, 0.15, 0.20$ compared to that of only Ti doped $\text{BiFe}_{1-x}\text{Ti}_x\text{O}_3$ ($x = 0.00 - 0.35$) ceramics observed in reference 6. Hence, it is clear that Gd and Ti co-doped

$\text{Bi}_{0.9}\text{Gd}_{0.1}\text{Fe}_{1-x}\text{Ti}_x\text{O}_3$ ceramics exhibit enhanced magnetic properties at RT showing weak ferromagnetic (WFM) antiferromagnetism.

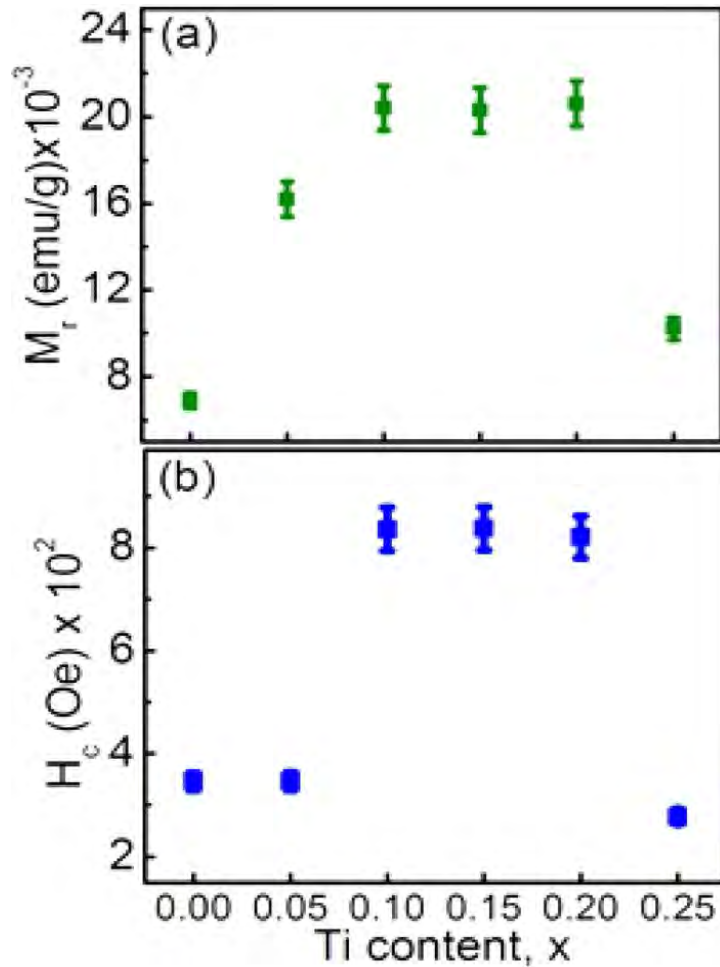


Figure 4.6: Variation of (a) remanent magnetization and (b) coercive fields at RT, respectively, in $\text{Bi}_{0.9}\text{Gd}_{0.1}\text{Fe}_{1-x}\text{Ti}_x\text{O}_3$ ($x = 0.00 - 0.25$) as a function Ti concentration.

The origin of WFM [26] due to a change in bond angle of Fe – O – Fe as a result of distortion created by Ti doping. The statistical distribution of Fe^{3+} and Fe^{2+} (created due to charge compensation) ions in the octahedral also lead to an increase in magnetization and weak ferromagnetism. However, for 25% Ti doping in $\text{Bi}_{0.9}\text{Gd}_{0.1}\text{Fe}_{1-x}\text{Ti}_x\text{O}_3$, the remanent magnetization and coercive field both again decreased and the antiferromagnetic order typical to BiFeO_3 parent phase is likely to be recovered. This

might be associated with the structure phase transition from rhombohedral to orthorhombic at $x = 0.25$ [6].

Notably, from FESEM images (Figure 4.2(b)), the average grain size was smallest (~200 nm) for Gd and Ti co-doped samples with $x = 0.10$, $x = 0.15$ and $x = 0.20$ for which the remanent magnetization and coercive fields are the highest as shown in figures 4.6(a) and 4.6(b). The dielectric constant over a wide range of high frequencies (50 kHz to 20 MHz) was also highest for these three samples compared to that of the other two samples. Therefore, the observed results clearly indicate that the dielectric and magnetic properties of Gd and Ti co-doped samples are related to the microstructure of the compositions.

Beside, this enhanced room temperature magnetic properties in Gd and Ti co-doped $\text{Bi}_{0.9}\text{Gd}_{0.1}\text{Fe}_{1-x}\text{Ti}_x\text{O}_3$ ceramics, the most intriguing feature observed from the enlarged view (Figure.4.5 (d) – 4.5 (f)) of the low-field M-H hysteresis loops is their asymmetric behavior. An asymmetry exhibiting shifts both in the field and magnetization axes can be clearly observed for all the samples. This indicates the presence of exchange bias (EB) effect in these compounds. The exchange bias effect usually occurs in ferromagnetic and antiferromagnetic bilayers or multilayers in which the two coercive fields of the magnetic hysteresis loop are not symmetric, and the centre of the magnetic hysteresis loop shifts to the left or right [22,23,27]. Recent investigations also demonstrate that the exchange bias effect can also exist in compounds or composites which allow the coexistence of both a ferromagnetic component and an antiferromagnetic component [22,27,28]. In compounds like NdMnO_3 [27] or $\text{La}_{1-x}\text{Pr}_x\text{CrO}_3$ [28], the exchange bias effect is different from what appears in bilayer and other interface structures.

The EB field H_{EB} is generally defined as $H_{\text{EB}} = - (H_{\text{c1}} + H_{\text{c2}})/2$ where H_{c1} and H_{c2} are the left and right coercive fields, respectively as shown by solid circles in figure 4.5 (h) [22,23]. The asymmetry in the magnetization axes is defined as $M_{\text{EB}} = (M_{\text{r1}} + M_{\text{r2}})/2$ where M_{r1} and M_{r2} are the magnetization with positive and negative points of intersection with $H = 0$, respectively [21]. Calculated values of H_{EB} and M_{EB} for different doping concentrations observed at RT are inserted in table 4.2. The exchange bias phenomena were also reported in a similar multiferroics $\text{La}_{0.8}\text{Bi}_{0.2}\text{Fe}_{1-x}\text{Mn}_x\text{O}_3$ as a function of Mn doping at 20 K, 100 K, and 200 K [3]. The presence of EB phenomenon in these

compounds was assumed to be associated with induced exchange anisotropy at the interface between FM and AFM phases [21]. For a comparison the calculated values of H_{EB} observed at 200K for multiferroics $La_{0.8}Bi_{0.2}Fe_{1-x}Mn_xO_3$ (Ref. 21) have been displayed in table 4.2 along with the values observed at RT for $Bi_{0.9}Gd_{0.1}Fe_{1-x}Ti_xO_3$ ($x = 0.00 - 0.25$) ceramics.

Table 4.2: The table shows the calculated values of H_{EB} and M_{EB} for $Bi_{0.9}Gd_{0.1}Fe_{1-x}Ti_xO_3$ ceramics observed at RT. Table also demonstrates comparison of the H_{EB} for $La_{0.8}Bi_{0.2}Fe_{1-x}Mn_xO_3$ multiferroics observed at 200K (Ref. 21) and $Bi_{0.9}Gd_{0.1}Fe_{1-x}Ti_xO_3$ ceramics observed at RT.

Ti concentration (x)	$Bi_{0.9}Gd_{0.1}Fe_{1-x}Ti_xO_3$ ceramics at RT		$La_{0.8}Bi_{0.2}Fe_{1-x}Mn_xO_3$ multiferroics at 200K (Ref. 21)	
	H_{EB} (Oe)	$M_{EB} \times 10^{-4}$ emu/g	Mn concentration (x)	H_{EB} (Oe)
0.00	00 ± 0.00	0.00 ± 00	0.2	+24
0.05	16 ± 0.8	15 ± 0.8	0.3	+08
0.10	06 ± 0.3	04 ± 0.2	0.4	-37
0.15	06 ± 0.3	05 ± 0.25	–	–
0.20	-36 ± 02	-05 ± 0.25	–	–
0.25	26 ± 1.3	09 ± 0.45	–	–

From the table, it is evident that the exchange bias fields vary randomly as a function of Ti doping in $Bi_{0.9}Gd_{0.1}Fe_{1-x}Ti_xO_3$ ceramics as was also observed in $La_{0.8}Bi_{0.2}Fe_{1-x}Mn_xO_3$ (Ref. 21) due to Mn doping. It is expected that the EB in these system originate from the exchange interaction at the interfaces of weakly ferromagnetic and antiferromagnetic components [29]. The asymmetry in the M-H curve was also observed at RT with 10% Sm doping in a similar type of ceramics $Bi_{1-x}Sm_xFeO_3$ [30]. The authors reported that in this compound while most of the sample remain largely antiferromagnetic, regions in the Sm-doped $BiFeO_3$ sample become weakly ferromagnetic and their interaction results an asymmetric behaviour in the M-H curve although the effect was not observed for 20% Sm doping. However, in the present investigation, EB bias effect was observed at RT up to 25% Ti doping.

Reference:

- [1] Kumar, M., and Yadav, K. L., “Study of room temperature magnetoelectric coupling in Ti substituted bismuth ferrite system”, *J. Appl. Phys.* 100, 074111, 2006.
- [2] Agarwal, R. A., Ashima, S. S., and Ahlawat, N., “Structural transformation and improved dielectric and magnetic properties in Ti-substituted $\text{Bi}_{0.8}\text{La}_{0.2}\text{FeO}_3$ multiferroics”, *J. Phys. D: Appl. Phys.* 45, pp165001- 165010, 2012.
- [3] Bernardo, M. S., Jardiel, T., Peiteado, M., Mompean, F. J., Garcia- Hernandez, M., Garcia, M. A., Villegas, M., and Caballero, A. C., “Ti doping-driven magnetic and morphological changes in multiferroic ceramics of $\text{Bi}_{0.9}\text{La}_{0.1}\text{FeO}_3$ ”, *Chem. Mater.* 25, 1533, 2013.
- [4] Gu, Y. H., Wang, Y., Chen, F., Chan, H. L. W. and Chen, W. P., “Effects of Ba and Ti Codoping on Stoichiometric and Nonstoichiometric BiFeO_3 Multiferroic Ceramics”, *J. Appl. Phys.* 108, 094112, 2010.
- [5] Cui, Y. F., Zhao, Y. G., Luo, L. B., Yang, J. J., Chang, H., Zhu, M. H., Xie, D., and Ren, T. L., “Dielectric, magnetic, and magnetoelectric properties of La and Ti codoped BiFeO_3 ”, *Appl. Phys. Lett.* 97, 222904, 2010.
- [6] Kumar, M., Yadav, K.L., “Study of room temperature magnetoelectric coupling in Ti substituted bismuth ferrite system”, *J. Appl. Phys.* 100, pp074111-074114, 2006.
- [7] Kumar, M. M., Srinivas, A., and Suryanarayana, S. V., “Structure property relations in $\text{BiFeO}_3/\text{BaTiO}_3$ solid solutions”, *J. Appl. Phys.* 87, 855, 2000.
- [8] Yuan, G. L., Kishi, K. Z. B., Liu, J. M., Or, S. W. , Wang, Y. P. and Liu, Z. G., “Multiferroic Properties of Single-Phase $\text{Bi}_{0.85}\text{La}_{0.15}\text{FeO}_3$ Lead-Free Ceramics”, *J. Am. Ceram. Soc.* 89, pp 3136-3139, 2006.
- [9] Makhdoom, A. R., Akhtar, M. J., Rafiq, M. A., and Hassan, M. M., “Investigation of transport behavior in Ba doped BiFeO_3 ”, *Ceram. Int.* 38, 3829, 2012.
- [10] Ianculescu, A., Prihor, F., Postolache, P., Mitoeriu, L., Drgan, N., and Crian, D., “Preparation, Structural and Magnetic Properties of Mn-Doped $\text{La}_{0.1}\text{Bi}_{0.9}\text{FeO}_3$ Ceramics”, *Ferroelectrics* 391, 67, 2009.

- [11] Brinkman, K., Iijima, T., Nishida, K., Katoda, T., and Funakubo, H., “The influence of acceptor doping on the structure and electrical properties of sol-gel derived BiFeO₃ thin films”, *Ferroelectrics* 357, 35, 2007.
- [12] Chaodan, Z., Jun, Y., Duanming, Z., Bin, Y., Yunyi, W., Longhai, W., Yunbo, W., and Wenli, Z., “Processing And Ferroelectric Properties Of Ti-Doped BiFeO₃ Ceramics ”, *Integr. Ferroelectr.* 94, 31, 2007.
- [13] Dutta, D. P., Mandal, B. P., Mukadam, M. D., Yusuf, S. M., and Tyagi, A. K., “Improved magnetic and ferroelectric properties of Sc and Ti codoped multiferroic nano BiFeO₃ prepared *via* sonochemical synthesis”, *Dalton Trans.*, 43, 7838–7846, 2014.
- [14] Fang, L. A., Liu, J. A., Ju, S., Zheng, F. G., Dong, W., Shen, M. R., “Experimental and theoretical evidence of enhanced ferromagnetism in sonochemical synthesized BiFeO₃ nanoparticles”, *Appl. Phys. Lett.*, 97, pp 242501, 2010.
- [15] Hu, G. D., Cheng, X., Wu, W. B., and Yang, C. H., “Effects of Gd substitution on structure and ferroelectric properties of BiFeO₃ thin films prepared using metal organic decomposition”, *Appl. Phys. Lett.* 91, 232909, 2007.
- [16] Maxwell, J. C., “A Treatise on Electricity and Magnetism”, Clarendon Press, Oxford, 1873.
- [17] Wagner, K. W., Theor, Z., “Zur Theorie der unvollkommenen Dielektrika”, *Ann. Phys.* 40, 817, 1913.
- [18] Azough, F., Freer, R., Thrall, M., Cernik, R., Tuna, F., and Collison, D., “Microstructure and properties of Co-, Ni-, Zn-, Nb- and W-modified multiferroic BiFeO₃ ceramics”, *J. Eur. Ceram. Soc.* 30, 727, 2010.
- [19] Zhang, Q., Kim, C. H., Jang, Y. H., Hwang, H. J., and Cho, J. H., “Multiferroic properties and surface potential behaviors in cobalt-doped BiFeO₃ film”, *Appl. Phys. Lett.* 96, 152901, 2010.
- [20] Lebeugle, D., Colson, D., Forget, A., Viret, M., Bonville, P., Marucco, J. F., and Fusil, S., “Room-temperature coexistence of large electric polarization and magnetic order in BiFeO₃ single crystals”, *Phys. Rev. B* 76, 024116, 2007.

- [21] Anjum, G., Kumar, R., Mollah, S., Shukla, D. K., Kumar, S., Lee, C. G., “Structural, dielectric, and magnetic properties of $\text{La}_{0.8}\text{Bi}_{0.2}\text{Fe}_{1-x}\text{Mn}_x\text{O}_3$ ($0.0 \leq x \leq 0.4$) multiferroics”, *J. App. Phys.*, Vol-107, pp-103916-103924, 2010.
- [22] Guo, Y., Shi, L., Zhou, S., Zhao, J., Wang, C., Liu, W., and Wei, S., “Tunable exchange bias effect in Sr-doped double perovskite $\text{La}_2\text{NiMnO}_6$ ”, *J. Phys. D: Appl. Phys.* 46, 175302, 2013.
- [23] Muthu, S. E., Singh, S., Thiagarajan, R., Selvan, G. K., Rao, N. V. R., Raja, M. M., and Arumugam, S., “Influence of Si substitution on the structure, magnetism, exchange bias and negative magnetoresistance in $\text{Ni}_{48}\text{Mn}_{39}\text{Sn}_{13}$ Heusler alloys”, *J. Phys. D: Appl. Phys.* 46, 205001, 2013.
- [24] Uniyal, P., Yadav, K.L., “Study of dielectric, magnetic and ferroelectric properties in $\text{Bi}_{1-x}\text{Gd}_x\text{FeO}_3$ ”, *Materials Letters* 62, pp 2858-2861, 2008.
- [25] Manoj, K., Prakash, C. S., Sandeep, C., “Electron spin resonance study and improved magnetic and dielectric properties of Gd–Ti co-substituted BiFeO_3 ceramics”, *J Mater Sci: Mater Electron*, 25:5366–5374, 2014.
- [26] Qi, X., Dho, J., Tomov, R., Blamire, M. G., and MacManus-Driscoll, J. L., “Greatly reduced leakage current and conduction mechanism in aliovalent-ion-doped BiFeO_3 ”, *Appl. Phys. Lett.* 86, 062903, 2005.
- [27] Hong, F., Cheng, Z., Wang, J., Wang, X., and Dou, S., “Positive and negative exchange bias effects in the simple perovskite manganite NdMnO_3 ”, *Appl. Phys. Lett.* 101, 102411, 2012.
- [28] Yoshii, K., “Positive exchange bias from magnetization reversal in $\text{La}_{1-x}\text{Pr}_x\text{CrO}_3$ ($x \sim 0.7-0.85$)”, *Appl. Phys. Lett.* 99, 142501, 2011.
- [29] W. H. Meiklejohn, W. H. and Bean, C. P., “New Magnetic Anisotropy”, *Phys. Rev.* 102, 1413, 1956.
- [30] Maurya, D., Thota, H., Garg, A., Pandey, B., Chand, P., and Verma, H. C., “Magnetic studies of multiferroic $\text{Bi}_{1-x}\text{Sm}_x\text{FeO}_3$ ceramics synthesized by mechanical activation assisted processes”, *J. Phys.: Condens. Matter* 21, 026007, 2009.

Chapter 5

Conclusions

5.1 Conclusions

The nominal compositions of $\text{Bi}_{0.9}\text{Gd}_{0.1}\text{Fe}_{1-x}\text{Ti}_x\text{O}_3$ ($x = 0.00 - 0.25$) ceramics were synthesized and their structural, morphological, dielectric and magnetic properties at room temperature were investigated. The combined effects of Gd and Ti doping in BiFeO_3 inhibit grain growth and stabilize dielectric constant over a wide range of high frequencies by suppressing dispersion at low frequencies. At high frequencies, dielectric loss attained minimum values which indicate the potential applicability of Gd and Ti co-doped BiFeO_3 ceramics in high-frequency microwave devices. Due to the substitution of Ti in $\text{Bi}_{0.9}\text{Gd}_{0.1}\text{Fe}_{1-x}\text{Ti}_x\text{O}_3$ ($x = 0.00 - 0.25$) ceramics, the remanent magnetizations and coercive fields were enhanced at room temperature. This enhancement of the room temperature magnetization might be attributed to the structural distortion in the perovskite with change in Fe – O – Fe angle due to Ti doping. Our investigation revealed that for Gd and Ti co-doped $\text{Bi}_{0.9}\text{Gd}_{0.1}\text{Fe}_{1-x}\text{Ti}_x\text{O}_3$ ceramics with $x = 0.10, 0.15,$ and $0.20,$ the average grain size is smallest, the dielectric constant at high frequencies is highest, the remanent magnetizations and coercive fields are also highest compared to that of the compounds with $x = 0.05$ and 0.25 . Therefore, it may be concluded that in these co-doped ceramics 10 to 20% Ti doping is optimum to have better multiferroic properties. The presence of exchange bias effect in these compounds at room temperature is another fascinating feature which was also reported in similar systems [1, 2, 3, 4] although at low temperature.

5.2 Future Work

In this investigation, we studied structural, dielectric and magnetic properties of Gd and Ti co-doped BiFeO_3 multiferroics and observed improved morphological, dielectric and magnetic properties at room temperature. It might be interesting to investigate further the temperature dependent dielectric and magnetic properties of Gd and Ti co-doped BiFeO_3 multiferroic ceramics. From temperature dependent magnetization experiments the exchange bias (EB) effect in this multiferroic system would be measured in details by

varying cooling field and temperature, which will be useful in spintronic device applications.

It might be interesting and equally important to prepare magnetic $\text{Bi}_{0.9}\text{Gd}_{0.1}\text{Fe}_{1-x}\text{Ti}_x\text{O}_3$ nanoparticles by using a physical technique like ultrasonication of multiferroic bulk material. In the mean time, an investigation was carried out and the results were reported in reference 5. From the XPS measurements, it was clearly observed the complete reduction of oxygen related defects e.g. oxygen vacancies in the fabricated nanoparticles, figure 5.1. The absence of oxygen vacancies might reduce the leakage currents [6] and therefore, we may expect improved ferroelectric properties of the synthesized nanoparticles in subsequent investigations.

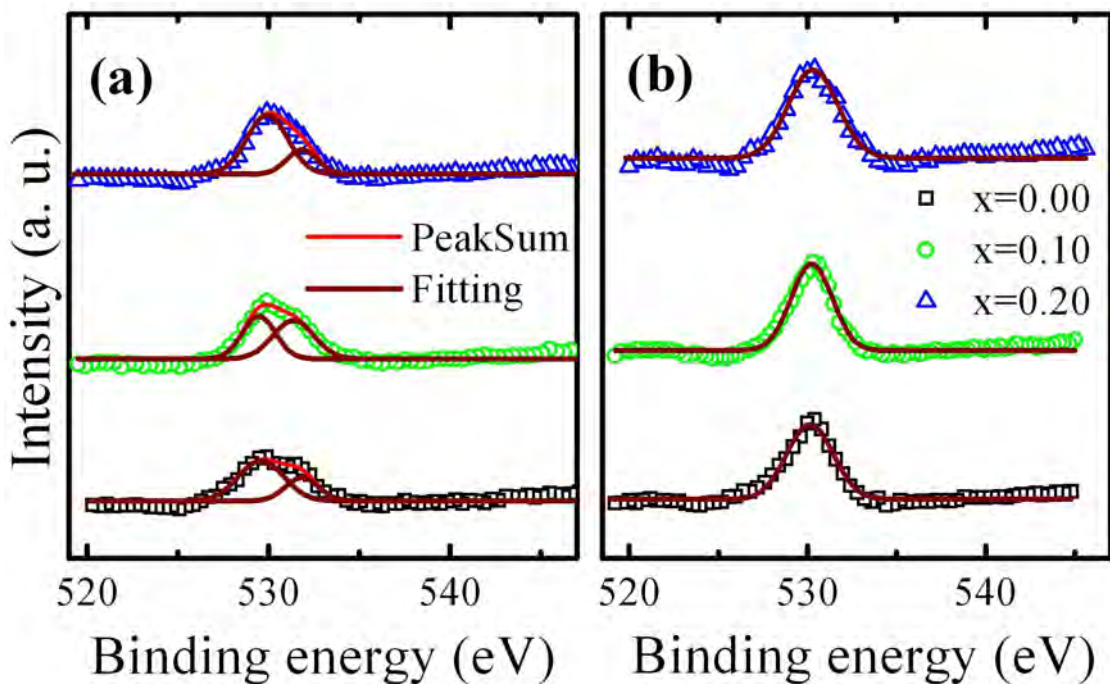


Figure 5.1: XPS spectra of the O 1s of $\text{Bi}_{0.9}\text{Gd}_{0.1}\text{Fe}_{1-x}\text{Ti}_x\text{O}_3$ ($x = 0.00 - 0.20$) (a) bulk polycrystalline materials and (b) nanoparticles obtained after a sonication time of 60 minutes. The oxygen related defects were completely reduced in the synthesized nanoparticles.

Reference:

- [1] Anjum, G., Kumar, R., Mollah, S., Shukla, D. K., Kumar, S., and Lee, C. G., “Structural, dielectric, and magnetic properties of $\text{La}_{0.8}\text{Bi}_{0.2}\text{Fe}_{1-x}\text{Mn}_x\text{O}_3$ ($0.0 \leq x \leq 0.4$) multiferroics”, J. App. Phys., Vol-107, pp-103916-103924, 2010.
- [2] Guo, Y., Shi, L., Zhou, S., Zhao, J., Wang, C., Liu, W., and Wei, S., “Tunable exchange bias effect in Sr-doped double perovskite $\text{La}_2\text{NiMnO}_6$ ”, J. Phys.D: Appl. Phys. 46, 175302, 2013.
- [3] Hong, F., Cheng, Z., Wang, J., Wang, X., and Dou, S., “Positive and negative exchange bias effects in the simple perovskite manganite NdMnO_3 ”, Appl. Phys. Lett. 101, 102411, 2012.
- [4] Yoshii, K., “Positive exchange bias from magnetization reversal in $\text{La}_{1-x}\text{Pr}_x\text{CrO}_3$ ($x \sim 0.7-0.85$)”, Appl. Phys. Lett. 99, 142501, 2011.
- [5] Basith, M. A., Ngo, D. T., Quader, A., Rahman, M. A., Sinha, B. L., Bashir Ahmmad, Fumihiko Hirose and Møhlhave, K., “Simple top-down preparation of magnetic $\text{Bi}_{0.9}\text{Gd}_{0.1}\text{Fe}_{1-x}\text{Ti}_x\text{O}_3$ nanoparticles by ultrasonication of multiferroic bulk material”, Nanoscale, 6, 14336, 2014.
- [6] Dutta, D. P., Mandal, B. P., Mukadam, M. D., Yusuf, S. M., and Tyagi, A. K., “Improved magnetic and ferroelectric properties of Sc and Ti codoped multiferroic nano BiFeO_3 prepared *via* sonochemical synthesis”, Dalton Trans., 43, 7838–7846, 2014.

- The End -